To the Graduate Council:

I am submitting here with a thesis written by Jing He entitled " A study of the electron beam scattering under various gaseous environment." I have examined the final electronic copy of this thesis for form and content and recommend that it be accepted in partial fulfillment of the requirements for the degree of Master of Science, with a major in Material Science and Engineering.

David C. Joy

_____

Major Professor

We have read this thesis
and recommend its acceptance:

R.A.Buchanan,

_____

Professor

Robert Mee,

_____

Professor

Accepted for the Council:

Anne Mayhew

_____

Vice Provost and Dean of Graduate Studies

(Original signatures are on file with official student records.)

A STUDY
OF THE ELECTRON BEAM SCATTERING
UNDER VARIOUS GASEOUS ENVIRONMENT

A Thesis Presented for the
Master of Science Degree

The University of Tennessee, Knoxville

Jing He

May 2003

DEDICATION

This thesis is dedicated to my loving husband, Hongbo Tian,
who has always been giving me strength and courage to achieve my goals; and
love and happiness to live a wonderful life.

I also dedicate this wok to my parents, Yao He and Yuhua Fan,
great role models, and without whose devotion and inspiration I will never be the
person I am today.

ACKNOWLEDGMENTS

Words can never express my deepest gratitude to my academic advisor Dr. D. C. Joy. Not only is he a distinguished scientist full of brilliant ideas, but also a wonderful instructor whose great enthusiasm, guidance, inspiration and support help me see and learn extraordinary things. I would also like to express my sincere appreciation to my committee members, Dr. R.A Buchanan and Dr. Robert Mee, for being highly supportive and instructive on my master program.

I wish to thank everybody in our EM lab, for making my time as a graduate student here exceptional memorable. Truly thanks to Xiaohu Tang and Satya M. Prasad for their genuine friendship and always being there for me. Thanks to Mr. Toshihide Agemura for his strong technical support on the Scanning Electron Microscope and Mr. Douglas Fielden for mechanical parts processing. I would also like to thank Dr. Carolyn and Dr. John Dunlap for their grand helps in lab equipment and materials, and to Jennifer Trollinger for her kindness and continuous assistance on everything. My thanks also go to Dr. Yeong-Uk Ko, Young Choi and Alexander Thesen for their support.

I would also like to thank my family and all my friends for always believing in me, encouraging me and supporting me to make today possible.

ABSTRACT

There are three objectives in this work: to experimentally measure the profiles of electron beams scattered by interaction with a gas, to measure total scattering cross-sections for gases and to apply the cross-section data in a suitable Monte Carlo simulation to predict beam scattering profiles for comparison with experiment.

The experimentally measured profiles cover a wide range of intensity variation. There are two evidenced regions: an inner region and an outer skirt corresponding to inelastic (small angle) and elastic scattering respectively are appeared. These profiles use the planar p-n junction gives us an overall look at the electron beam spreading, including the oversize and shape of the profile.

The experimental total scattering cross-section data obtained is of great interest. It shows the excellent agreement between experimental values and theoretical estimates of the total gas scattering cross-section and also confirms the predicted linear relationship between log (I_p/I_0) and gas pressure. On the basis of the available evidence, gases tend to be molecular rather than atomic in nature in the pressure range used.

The experimentally collected gas scattering cross-section data eventually was inserted into Monte Carlo simulation program. The established Monte Carlo simulation predicts the spatial distribution of the electron beam scattering under given beam energy and various other experimental conditions. The resulted beam profiles from the simulation are well agreed with the experimental measured profiles, with much higher accuracy and more variety of experimental conditions choices.

TABLE OF CONTENTS

Chapter			Page
I.	**INTRODUCTION**		1
	1.1	Electron Microscopy	1
	1.2	Scanning Electron Microscopy	1
	1.3	Gaseous Environmental Scanning Electron Microscope	4
		1.3.1 Gaseous Environmental SEM	4
		1.3.2 Charge Compensation by Gas	6
		1.3.3 Direct Examination of Dirty and Wet Sample	9
		1.3.4 Selectively Etching and Deposition by E-beam	9
	1.4	Electron Beam Scattering	14
		1.4.1 Scattering Introduction	14
		1.4.2 Electron Beam Scattering by Gas	15
		1.4.3 Gas scattering Cross-section Introduction	18
		1.4.3.1 Definition of Cross-section	18
		1.4.3.2 Rutherford and Mott Cross-section	22
		1.4.3.3 Mean Free Path	23
II.	**DIRECTLY MEASUREMENT OF THE ELECTRON BEAM SCATTERING**		25
	2.1	Introduction	25
	2.2	Introduction of P-N Junction Solar Cell	25
	2.3	Experimental Method	26
	2.4	Experimental Procedure	29
	2.5	Experimental Results and Discussion	32
	2.6	Summary	32
III.	**MEASUREMENT OF TOTAL GAS SCATTERING CROSS-SECTION**		35
	3.1	Introduction	35
	3.2	Experimental Method	35

3.3 Experimental Procedure 37
3.4 Experimental Results 39
3.4.1 Linear Relationship of Ln (I) and P 39
3.4.2 Calculated Total Scattering Cross-sections 39
3.5 Discussion of Errors in the Procedure 49
3.5.1 Gas Pressure Measurement in the VPSEM 49
3.5.2 Confirmation of the Gas Path Length 51
3.5.3 Confirmation of the Temperature Variation 51
3.5.4 Possible Noise Signals from the Background 54
3.6 Experimental Results Discussion 56
3.7 Summary 59

IV. MONTE CARLO SIMULATION OF THE ELECTRON BEAM SCATTERING 61
4.1 Introduction of Monte Carlo Simulation 61
4.1.1 Background Introduction 61
4.1.2 Random Number Sampling 63
4.2 Monte Carlo Simulation of Electrons Trajectories in a Solid 63
4.2.1 Basic Principle 64
4.2.2 Assumptions for Original Model 66
4.2.3 Statistics of the Original Model 66
4.3 New Monte Carlo Simulation for Gas 69
4.3.1 Why Use This Method 69
4.3.2 How We Did It 70
4.3.2.1 Include Inelastic and Elastic Scattering 70
4.3.2.2 Single Scattering Model 71
4.3.2.3 Energy Loss of the Incident Electrons 78
4.3.2.4 Schematic Sequence of the Operation 79
4.3.2.5 I(r) Radial Beam Distribution Plot 79
4.3.2.6 Computer Code 81
4.4 Simulation Results 81
4.5 Summary 86

REFERENCES 89
APPENDIX 95
VITA 108

LIST OF FIGURES

Figure		Page
1.1	The comparison of SEM micrograph and optical micrograph of the adiolarian Trochodiscus longispinus.	2
1.2	A standard ESEM column configuration.	5
1.3	Relationship between incident beam energy and surface charging.	7
1.4	Schematic of the ionizing collisions in a low-pressure gas above a charged insulator.	8
1.5	IC examined in VPSEM under different air pressures.	10
1.6	Live cells and liquid specimen examined in ESEM.	11
1.7	E-beam deposition and etching for Silicon wafer.	12
1.8	Principle of EBD.	13
1.9	Schematic of scattering by a small particle.	14
1.10	Schematic of the scattering by surrounding gases in VPSEM.	17
1.11	The interaction cross-section for a particular process compared with the geometric cross-section.	20
1.12	Schematic of the differential cross-section calculation.	21
1.13	Mean free path and kinetic energy.	24
2.1	Band structures of differently doped semiconductors.	27
2.2	Band-bending structure of hetero-junction.	27
2.3	Principle of photovoltaic device.	28
2.4	Schematic arrangement of measuring the beam profile in a SEM.	30
2.5	SE image of the positioned solar cell.	31
2.6	AE image detected by the solar cell.	31
2.7	Raw profile data collected at 15, 20, 25keV.	33
2.8	Scattered beam profiles in Air at E = 25keV after deconvolution.	34
3.1	Schematic of the experimental technique.	36
3.2	Experimental equipment (VPSEM, EDS, Manometer).	38
3.3	SEM image of the Al wire cross-section.	40
3.4	Linear relationship of ln (I) and P for Air.	41
3.5	Linear relationship of ln (I) and P for Helium.	42

3.6	Linear relationship of ln (I) and P for Argon.	43
3.7	Linear relationship of ln (I) and P for Methane.	44
3.8	Linear relationship of ln (I) and P for gases at 15keV.	45
3.9	MKS Baratron® 626A capacitance manometer.	50
3.10	Pressure readings by capacitance manometer and Pirani gauge.	51
3.11	Comparison of the collected X-ray signals at two GPLs.	53
3.12	Background signals under 15keV and 20keV.	55
3.13	Comparison of theoretical and experimental cross-section for atomic Helium.	56
3.14	Theoretical cross-section for atomic and molecular Nitrogen.	58
3.15	Experimental cross-section for air compared to its components.	59
4.1	Calculation of π by Monte Carlo method.	62
4.2	Physics processes encountered by electron.	65
4.3	Monte Carlo simulation of the electron trajectories.	68
4.4	Schematic of the small angle scattering.	72
4.5	Coordinate system for Monte Carlo simulation.	74
4.6	Interface of the simulation.	80
4.7	Comparison of beam scattering in air and helium at E = 20keV, P = 30Pa.	82
4.8	Comparison of beam scattering at E = 10keV, 20keV, P = 30Pa in helium.	83
4.9	Comparison of beam scattering at P = 30Pa, 100Pa, E = 20keV in helium.	84
4.10	Comparison of beam scattering with Ratio (inelastic/elastic) = 0.1 and 0.15 at E = 20keV, P = 30Pa.	85
4.11	Comparison of beam scattering with Mott's cross-section and experimental cross-section applied, at E = 20keV and P = 30Pa in helium.	87
4.12	Comparison of the scattered electron beam radius obtained from the Monte Carlo model and P-N diode measurement in Air at E = 25keV.	88

CHAPTER I INTRODUCTION

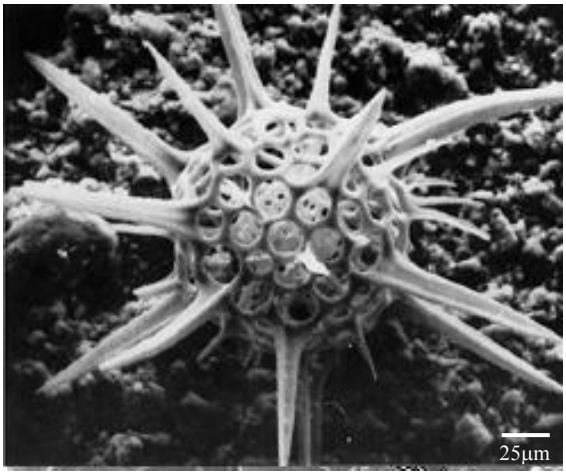
1.1 Electron Microscopy

Electron microscopy is a very powerful technique which permits scientists to observe, analyze and correctly explain phenomena occurring on a micrometer or submicrometer scale. Electron microscope is analagous to light microscope where the light beam is replaced by a beam of electrons. The electron beam is focussed by a series of electrostatic or electromagnetic lenses. The types of signals produced when the electron beam inpinges on a specimen sureface include secondary electrons, backscattered electron, Auger electrons, characteristic x-rays, and photons of various energies. These signals are obtained from specific emisssion volumes within the sample and can be used to examine many characteristics of the interested samples, such as compostition, surface topography and crystallography etc.

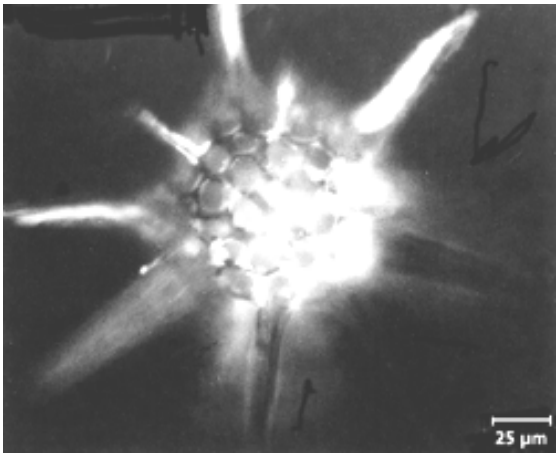
1.2 Scanning Electron Microscopy

The scanning electron microscopy (SEM) is one of the most versatile instruments available for the examination and anlysis of the microstructural characteristics of solid objects. In scanning electron microscopy the beam sweeps the surface of the sample synchronised with a beam from a cathode ray tube. The signals of greatest interest here are from secondary electrons and backscattered electrons. One of the major features of the SEM is that the resolution can reach as high as 1 nm, and another is the three dimensional appearance of the specimen image, due to the large depth of field as well as to the shadow-relief effect of the secondary and backscattered electron contrast. Compared with optical microscopy image, the image obtained in SEM has much greater depth of focus and superior resolving capability as illustrated in Figure 1.1.

The magnification of SEM is determined by the size of the scanned surface area in comparison to the size of the screen on which the image is projected, which is easy to adjust because the variation of the magnification is only related with the change of the geometry size of the image screen. Resolution depends on the size of the electron beam



(a)



(b)

Figure 1.1 The comparison of SEM micrograph and optical micrograph of the adiolarian Trochodiscus longispinus. (a) SEM image, (b) Optical image [Goldstein et al. 1992].

and on the scattering volume within the sample but the depth of focus is because the angle of convergence of the focussed beam is small.

One of the disadvantages for conventional scanning electron microscopes (SEM) is that operation under high vacuum ($<10^{-3}$Pa) is always strictly required, so sample to be investigated must be clean, dry and free of volatile species and electrically conductive. This has always been a limitation when the samples are materials with poor electrical conductivity, such as semiconductor, IC chips, fibers, or some live cells with water vapor components. Since these materials are playing a more and more important role in our everyday lives and are widely used in various technology fields, such as pharmaceuticas, fiber technology, cement science, medical, biology , entomology and microelectronics, a new generation of SEM is urgently required.

Why are there such limitations? What happens when we put such specimen inside the SEM chamber?

a. When an electron beam irradiates an insulator, a dielectric, or a semiconductor during SEM observation, stored charges will build up on the specimen. The contrast of the image thus may become abnormal and unstable, and the resolution of the image may degrade**.** Charge accumulation in insulator or semiconductor materials due to electron beam irradiation is one of the key problems in electron microscopy. Traditionally coating a thin conductive layer on the sample surface is an effective way to eliminate charging, but the coating may reduce topographic and chemical composition contrast, and obscure crystallographic channeling patterns [Moncrieff et al 1978]. Reducing the incident beam energy is another possible solution to charging since this can increase the SE yield from the sample until the charge injected by the beam is balanced by the charge (SE+BSE) emitted by the sample [Cazaux 1988]. However, lower beam energies may result in poorer resolution, and there are practical problems in applying this method to an inhomogeneous surface [Tang, 2002].

b. When a liquid and hydrated samples are directly examined inside the SEM chamber, it will destroy the high vacuum environment required by conventional SEM and also may contaminate the lenses and aperture in the system. Biological samples were always, therefore, dehydrated before they are put into the SEM specimen chamber, which results that the real characteristic of the sample can not be explored, and that live cells could never be observed in conventional SEM.

With the fast growing interests of all these advanced materials in this new era of science and technology, the electron microscopy technology is also developing rapidly to adapt all the materials studies which are unsuitable for conventional SEM.

1.3 Gaseous Environmental Scanning Electron Microscope

A very promising family of Scanning Electron Microscopes (SEM) is those with a low pressure of gas in the specimen chamber, such as the environmental scanning electron microscope (ESEM) or the variable pressure scanning electron microscope (VPSEM). These gaseous environment SEMs do not have the limitations on state of the specimen. These machines offer the ability to image insulators and wet, dirty or damp materials such as biological tissue, and even liquids without extra sample preparation and coating.

1.3.1 Gaseous environmental SEM

Gaseous environmental SEM operates at relatively high pressures while the vast majority of traditional microscopes operate at a vacuum below 10^{-2} pa. This includes a variety of techniques reported in the scientific and commercial literature, e.g., environmental scanning electron microscopy (ESEM) shown in Figure 1.2, low Vacuum SEM and Variable Pressure Scanning Electron Microscopy (VPSEM). The term high pressure scanning electron microscopy (HPSEM) is introduced by [Farley et al. 1990a,b] to distinguish these techniques from conventional high vacuum SEM[C. Mathieu 1999].

The conventional Everhart-Thornley detector cannot be used in the HPSEM because of electrical breakdown in the gas, so the following modes of detection have been employed: (a) specimen current and biased current mode, in which a biasing electrode is used above the specimen to influence the trajectories of the charge carriers and hence the image contrast. The specimen is connected, via the specimen stub, the virtual earth terminal of a charge-sensitive amplifier to collect the current generated in and around the specimen. (b) Emissive mode: employed by using a gaseous detector device (GSED) [Danilatos 1990a]. The GSED is a collecting electrode placed in the vicinity of the specimen and it is positively charged. The GSED collects ions produced by the emitted electrons, along with the electrons generated by the emitted and the

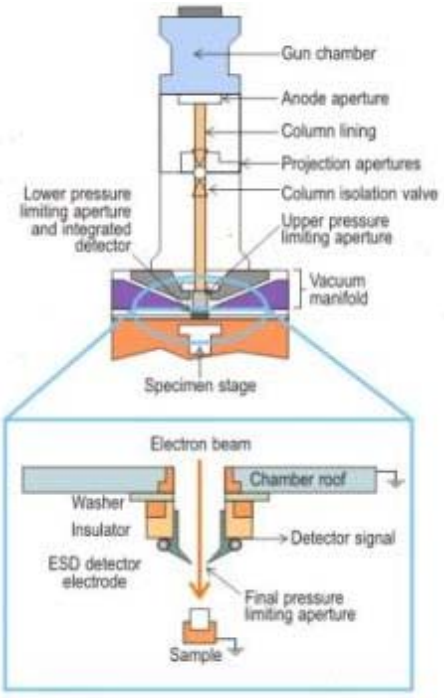


Figure 1.2 A standard ESEM column configuration [McDonald et al., 1998].

primary electrons. (c) Backscattered mode: Backscattered electron imaging with high gas pressure in the specimen chamber has proven to be a useful technique and this technique has been widely used in the Variable Pressure Scanning Electron Microscope (VPSEM) [Mathieu 1996].

1.3.2 Charge Compensation by Gas

The gaseous environmental SEM allows observations to be carried out in the presence of the low pressure gases. The gaseous environment inside the specimen chamber during operation consists of low-energy secondary electrons, gas molecules, and ions that have the added benefit of helping to drain the excess surface charge away [Wight 2001], because the ionizations which occur in the gas as the result of electron interactions produce a flux of positive ions which migrate to charged regions on the surface and neutralize them. The suggested mechanism for the charge neutralization by low pressure gases could be the continuous discharge by ionization currents resulting from ion pairs formed by electron collisions with gas molecules [Moncrieff et al. 1978]. The need for conductive coatings is therefore reduced or eliminated when these poorly conductive or insulator samples can be imaged at high beam energies (typically 10–30 keV) [Mohan et al. 1998].

As illustrated above, surrounding the sample with a low-pressure gas is a very efficient solution for the charging accumulation problem [Robinson 1978]. Figure 1.3 shows schematically the relationship between incident beam energy and surface charging under vacuum condition and a fixed gas pressure, which indicates that the gas inside the chamber plays an important role on the charging behavior. At all incident beam energies the presence of an atmosphere of gas efficiently reduces the surface potential from typically thousands of volts to just a few hundred volts. Similar observations have also been made in XPS experiments [Yu et al. 1990] but using a localized jet of gas.

Incident primary electrons (PE), secondary electrons (SE), and back-scattered electrons (BSE) can interact with gas molecules and produce positive and negative ions. The positive ions will flow to negatively charged regions while the negative ions will go to positively charged areas so as to neutralize surface build-up charge. The electric field off the sample surface due to charging and bias on the electrode accelerates the negative ions, initiating a gas ionization cascade (Figure 1.4), which further enhances the charge

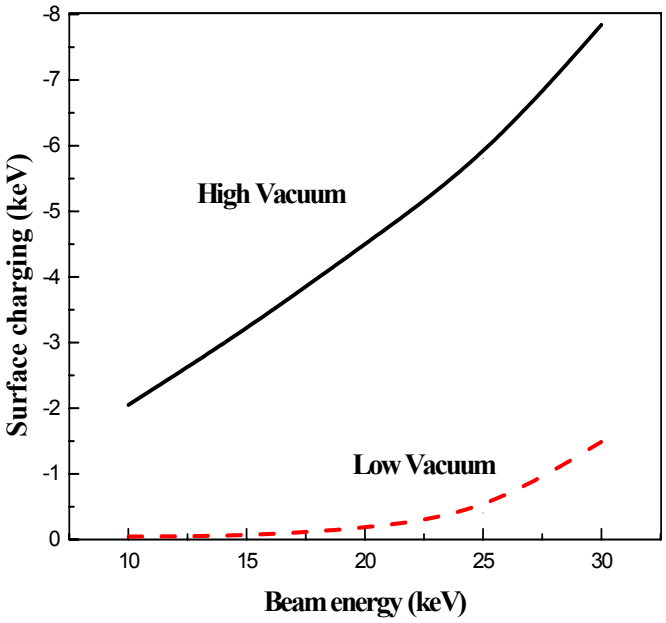


Figure 1.3 Relationship between incident beam energy and surface charging.

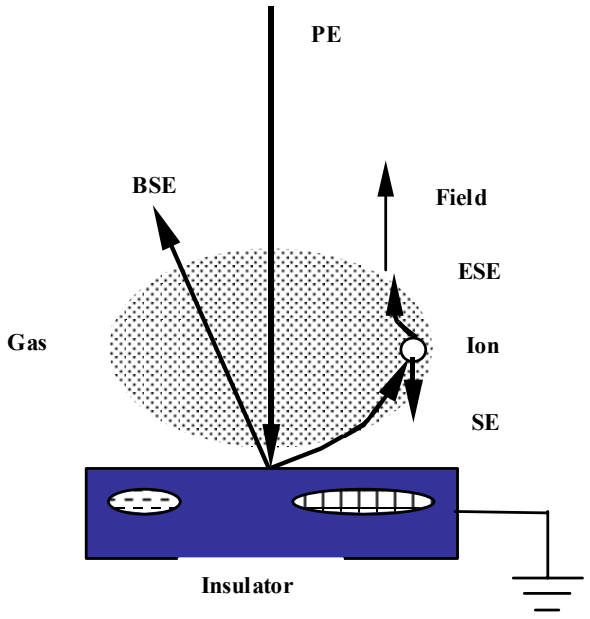


Figure 1.4 Schematic of the ionizing collisions in a low-pressure gas above a charged insulator.

compensation. Charge carriers in the gas are PE, BSE, SE, ionized gas molecules, electrons liberated as a consequence of ionizing collisions involving gas molecules (ESE) and electrons liberated by positive ions impact on the sample surface (ESE). The major contribution to the gas cascade comes from the SE emanating from the sample surface due to their low energy [Toth et al. 2000]. On the other hand, the positive ions have a much higher mass than electrons so that their mobility is lower than electron, and an ion-gas collision is easier than an electron-gas collision. These two kinds of particles can effectively neutralize the charging surface. All the factors above induce the gas ionization avalanche, producing ion current, which takes charge of the charging neutralization. The charging neutralization is apparent in Figure 1.5, where the same IC chip is examined under the same incident beam energy of 15keV, magnification of 45x and working distance of 12mm but under different amount of air atmosphere.:

1.3.3 Direct Examination of Dirty and Wet Sample

In the gaseous environmental SEM, it is also possible to image samples that are dirty, moist, or even wet without causing any damage for the vacuum system, because a Pressure Limiting Aperture (PLA) prevents the flow of gas to the gun. Meanwhile we can now directly observe the interested hydrated sample under electron beam without losing any information which may be caused by dehydration and obtain real images of live cells. As shown in Figure 1.6, vivid image of the live cells and even of liquid can be obtained in a gaseous environmental SEM.

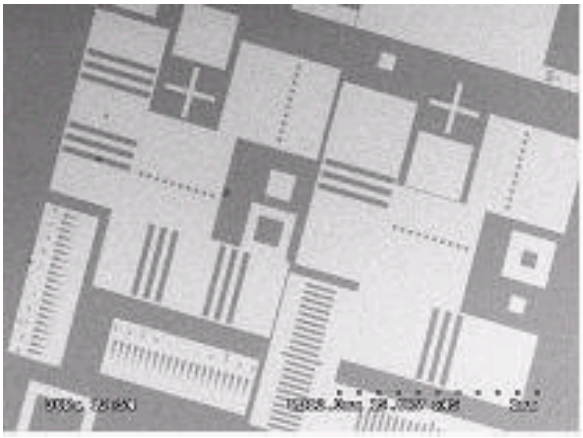
1.3.4 Selectively Etching and Deposition by E-beam

The interaction between the incident electron and the gas can also be used to selectively etch or deposit materials (Figure 1.7). This new technique is causing the enormous attention of semiconductor and microelectronics industry.

Conventional deposition techniques used in the fabrication of micron or sub-micron structures e.g., microelectronics devices, do not allow the deposition of materials on a very small area of the substrate. Instead, materials are deposited over the whole substrate and the pattern is defined afterwards by removing material from the adjacent

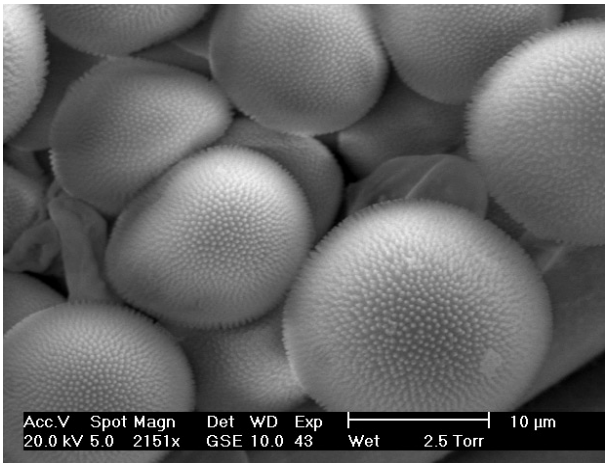


(a)

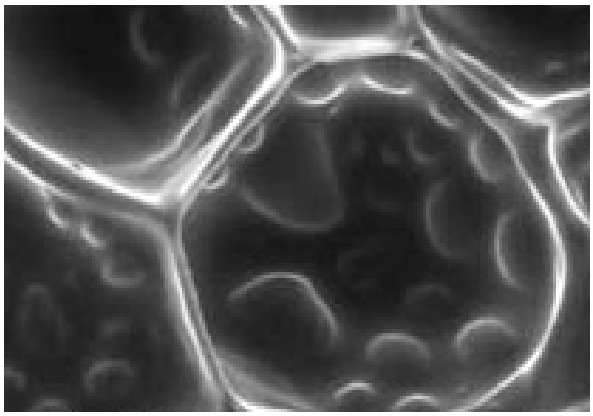


(b)

Figure 1.5 IC examined in VPSEM under different air pressures. (a) 0 Pa, (b) 30 Pa.

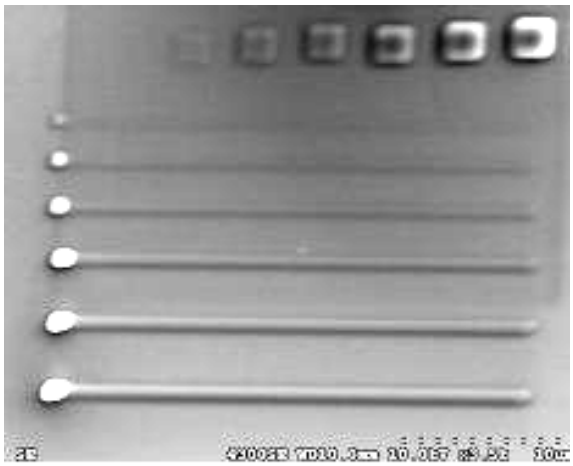


(a)



(b)

Figure 1.6 Live cells and liquid specimen examined in ESEM. (a) Spore, (b) Cell water.
Source: http://www.feic.com/esem/gal4.html



(a)



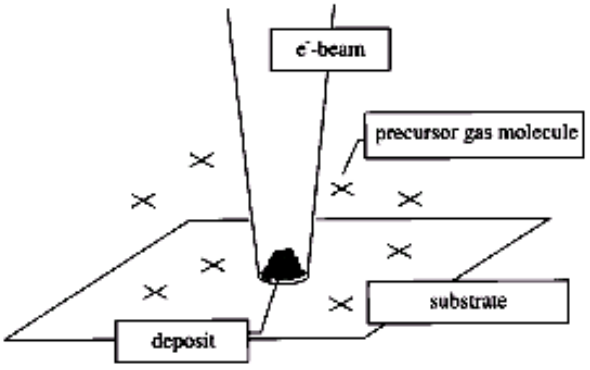
(b)

Figure 1.7 E-beam deposition and etching for Silicon wafer. (a) Deposition on Si wafer using $W(CO)_6$ under 10keV, 0.2Pa , (b) Etching of Si wafer using XeF_2 under 10keV, 0.1 Pa.

resists, photo- or electron-beam lithography, lift-off, and/or selective etching which result in costly processes and generally require planar substrates [Folch 1996].

Electron beam deposition (EBD) is a novel method (Figure 1.7) for directly applying the desired material on only a very small area of a substrate (selective deposition) at low temperature. This represents an attractive application of electron beam induced chemical reaction at a gas-substrate interface [Matsui 1986)]. In the presence of a surrounding gas, a finely focused electron beam is observed to cause the deposition of material from the gas only in the area irradiated by the beam. Nanometer structures can be fabricated by electron beam induced surface reaction, because beam diameters, as small as 0.5 nm, can be formed with conventional electron optical equipment [Broers 1976)]. In EBD, materials are patterned and deposited *simultaneously*, so it is an inexpensive technique due to its maskless and resistless. The technique of EBD is suitable for the fabrication of structures of different sizes, shapes, and materials in the sub-micron or nanometer scale.

Directly etching is also possible by using the electron beam induced surface reaction. Coburn et al. [1987] reported Si, SiO_2 and Si_3N_4 etched by electron beam induced reactions using an XeF_2 gas source that Matsui [Matsui 1987] reports that W deposition from WF_6 took place at SiO_2 substrate of temperature below 50ºC but etching occurred when temperature higher than 50ºC.



A focused e^- beam induces a chemical change on the precursor gas molecules that are adsorbed on the irradiated spot.

Figure 1.8 Principle of EBD

The deposition rate depends on the total e-beam current density at the beam spot, on the effective absorption rate of the precursor gas molecules onto the substrate, and on the probability for an electron to cause EBD of a molecule. In addition, the beam current density depends not only on the beam spot size but also on the rate of emission of secondary and backscattered electrons, which also contribute to the process [Matsui 1989].

1.4 Electron Beam Scattering

For all of these reasons there is, therefore, growing interest in understanding the problem of performing scanning microscopy in the presence of a low pressure of gas. One of the most important problems is the fact that the electron beam is scattered by its interactions with the gas.

1.4.1 Scattering Introduction

"Scattering", refers to the case of a beam of incident radiation striking a small particle (an atom or cluster of atoms acting as a unit) and giving rise to an angular distribution of emergent radiation as indicated in Figure 1.9, which depends on the nature of the individual - incoherent scattering case. The intensity distribution is the sum of the intensities given by the individual particles acting independently. Electrons are scattered much more strongly by matter than X-rays or visible light.

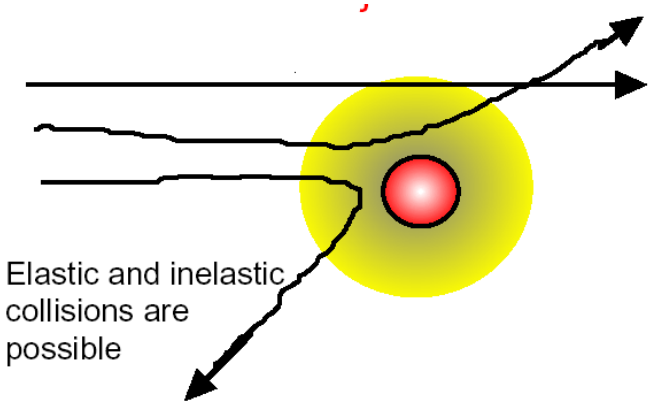


Figure 1.9 Schematic of scattering by a small particle.

Collisions between objects are governed by laws of momentum and energy. When a collision occurs in an isolated system, the total momentum of the system of objects is conserved. Provided that there are no net external forces acting upon the objects, the momentum of all objects before the collision equals the momentum of all objects after the collision. If there are only two objects involved in the collision, then the momentum change of the individual objects are equal in magnitude and opposite in direction.

Certain collisions are referred to as elastic collisions. Elastic collisions are collisions in which both momentum and kinetic energy are conserved. The total system kinetic energy before the collision equals the total system kinetic energy after the collision. If total kinetic energy is not conserved, then the collision is referred to as an inelastic collision.

1.4.2 Electron Beam Scattering by Gas

In SEM, when the electron beam strikes the specimen, there are a host of possible reactions or interactions between the primary electron beam and the specimen, and their study has constituted a fundamental topic of electron microscopy [Mathieu, 1999]. Thus, a primary electron may undergo elastic or inelastic collisions in the specimen resulting in the generation of secondary (SE) or backscattered electrons (BSE), X-rays etc., and changes in the specimen by molecular scission or cross linking. All of these different interactions are characterized by the fact that they occur between two entities: the beam and the specimen.

By allowing gas around the specimen, the number and the type of reactions are multiplied and it is helpful if these reactions are classified and studied in a logical manner according to some natural distinction. Four main entities and be distinguished which interact with each other: Beam, gas, specimen and signals [Danilatos 1990b]. Therefore the large number of reactions can be subdivided into six general types of interactions. These general types are not independent from each other and thy may influence each other.

Beam-specimen interactions: result in (1) beam scattering, which determines the interaction volume (2) generation of signals (3) modification of the nature of the specimen (beam irradiation effects).

Beam-gas interactions: result in (a) scattering of the beam, (2) generation of signals such as SE, BSE, X-rays and photons. (3) Modification of the gas due to the creation of positive and negative ions, dissociation products and excited molecules.

Specimen-signal interactions: results primarily in signal modifications and, to a minor extent, in specimen modification. One example for signals modified by the specimen is that secondary electrons are modified by a charged surface, or BSE by topographic undulations. Signal-gas interactions: results a mutual modification both of the signal and the gas. This type of interaction is of extreme significance in the VPSEM and is an important area of investigation. Gas-specimen interactions: are as expected from the general physical-chemical reactions in studies outside electron microscopy. Beam-signal interaction: beam can affect the signals indirectly through its interaction with the gas (the background noise).

Among these interactions, beam-specimen and beam-gas interactions are most important and most used interactions nowadays. Both these interactions could result in scattering of electron beam, but one difference we should notice is that scattering due to Beam-specimen interaction happens inside the sample, while the scattering due to Beam-gas interaction take place before the electron beam impinge the specimen surface. There are extensive established theories, computer simulations, and a significant literature on beam-specimen interactions, so researchers have a clear concept of how the electrons being scattered after their collision of the specimen. But the scattering of the primary electron beam by the gas molecules is not well understood, so more beam-gas interaction related theoretical and experimental studies are extremely necessary, especially this type of interaction is causing more and more attentions because of the fast development of the gases involved micro-scale production in the microelectronics and the semiconductor industries. For this reason we concentrate on electron beam-gas scattering research in our project.

In the electron microscope system with the presence of the low pressure gases, the incident electron beam is scattered by the gas molecules (Figure 1.10), forming the so-called ‘skirting’ [Schumacher 1968], when it travels through gas to reach the specimen. These electrons scattered out of the primary electron beam are a consequence of the high-volume density of gas molecules in the gaseous environmental SEM. In the case of imaging with backscattered or secondary electrons the skirt electrons contribute a nonspecific signal that acts to increase the noise and degrade the signal-to noise ratio.

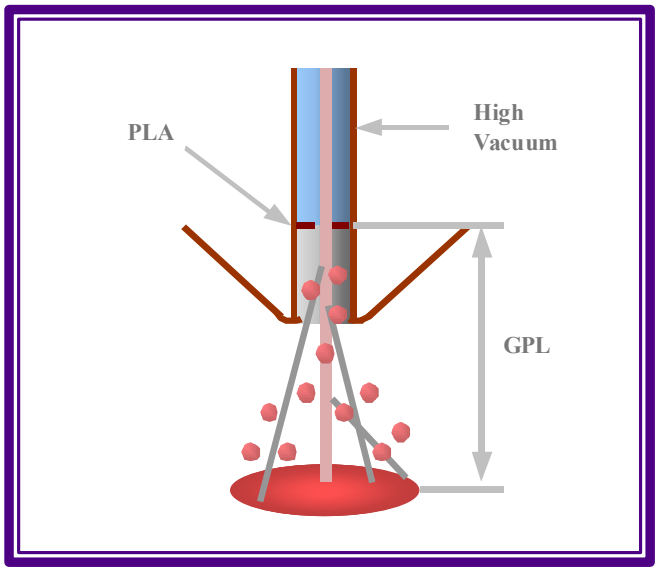


Figure 1.10 Schematic of the scattering by surrounding gases in VPSEM.

Also a chemical characterization problem could arise when those X-rays generated by the scattered electrons from a nearby material that is different in composition from the interested material under the primary beam. Consequently the quality of the images of the samples, or quality of the deposition, or etching during the micro processing, are all directly limited by this factor, the scattering of the electron in the primary beam by the gas [Stowe et al. 1998]. Therefore gas scattering of electrons must be considered here while it has never been an issue in the conventional SEM.

Electron beam scattering is also classified as being elastic, when only negligible electron energy transfer to the nucleus of the atom takes place, in the electron energy range used in the SEM, or inelastic when the fast incident electron interacts with the inner- or outer-shell atomic electrons [Egerton 1996] and lose relative large amount of electron energy.

1.4.3 Gas Scattering Cross-section Introduction

It is necessary to understand qualitatively and quantitatively how the electron beam is scattered so that we could accurately utilize the electron-gas interactions and minimize the problems these interactions could cause. The amount of scattering of the primary beam is dependent on a number of factors including electron beam cross-section, working distance, gas pressure, gas composition, and accelerating voltage of the SEM [Stowe et al. 1998].

The skirt electrons could contribute to a loss of contrast, beam current and so gas scattering cross-section. For understanding how the electron beam scattered by presented gas molecules, the gas scattering cross-sections is one of the most essential information used to since it is a measurement for the magnitude of the electron beam scattering. It is a paramount important parameter in electron beam study because this value makes it possible to calculate the details of the electron distribution resulting from the collisions of electrons with gas molecules or atoms. For example, the total cross-section can be used in a suitable Monte Carlo simulation [Joy 1995, 1996] designed to simulate the spatial distribution of the electrons striking the sample after passage through the gas.

1.4.3.1 Definition of Cross-section

When an incident beam traverses the target some of the particles may be scattered from their original direction by interaction with the nuclei in the target. The probability that an incident particle will undergo a specified type of interaction is proportional to n, the number of target particles per unit area in the foil. If the probability is σn, then each target particle presents an effective cross-sectional area σ (Figure 1.11). The probability σn is a dimensionless number, so with the unit of (unit area)$^{-1}$ for n, then σ must have the dimension of an area. If we assume that σn <<1 there is no overlap of these cross-sectional areas. This is equivalent to keeping a target rather thin or using a gaseous target has a sufficiently low density. At this point the cross-section for scattering, σ, means that a fraction σn of the incident particles is scattered. It is easier to understand by visualizing the cross-section as a geometric area, then if any particle incident upon the target hits the target inside this area it will be scattered, and if it impinges outside this area it will traverse the target undeflected. The total scattering cross-section is the sum of elastic and inelastic scattering cross-sections. Elastic scattering involves those processes where the incident particles are deflected from their initial directions without losing energy. Inelastic scattering involves those processes in which energy losses from the incident particles occur, i.e., the incident particle may excite a target nucleus into a higher energy state.

The scattering cross-section just defined above determines the number of particles that undergo a scattering event when a beam is incident upon a target, but it doesn't provide any information regarding the direction of the scattered particles. In order to obtain that information a differential cross-section with a solid angle will always be studied. As indicated in Figure 1.12, when the area dσ (the area into which the particle is incident on) increased, the area into which it scatters dΩ increases. The differential cross-section here is the proportionality factor D(θ) which gives the angular information about the scattering as we mentioned. It typically depends only on the scattering angle θ for spherically symmetric potentials. With $d\sigma = \left| bdbd\phi \right|$, $d\sigma = \left| \sin\theta d\theta d\phi \right|$, the differential cross-section is then

.

$$D(\theta) \equiv \frac{d\sigma}{d\Omega} = \left| \frac{b}{\sin\theta} \left(\frac{db}{d\theta} \right) \right| \qquad 1.1$$

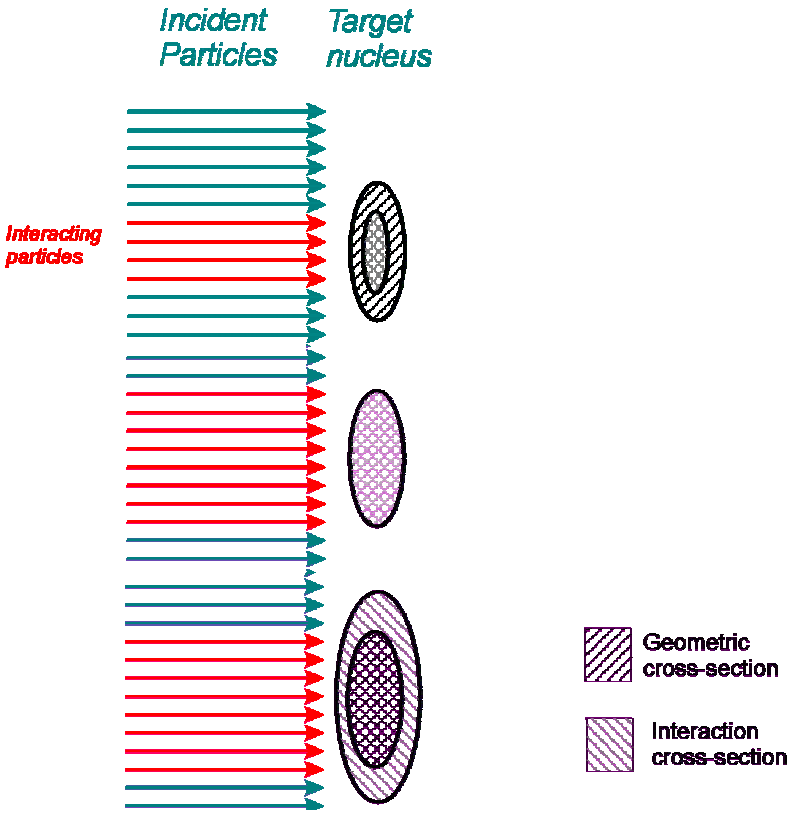


Figure 1.11 The interaction cross-section for a particular process compared with the geometric cross-section [Hunt, 2000].

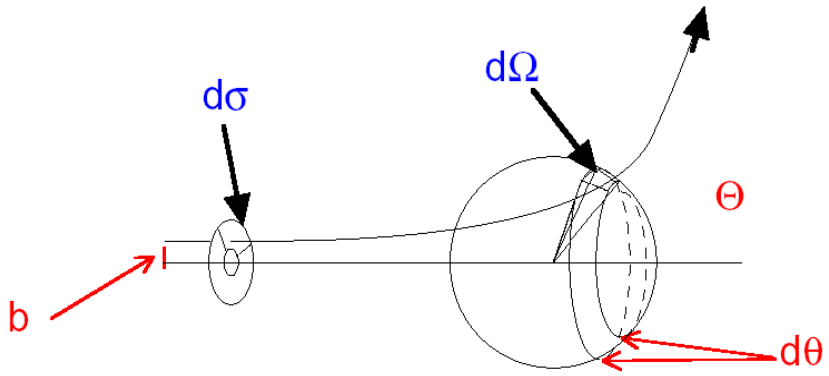


Figure 1.12 Schematic of the differential cross-section calculation.

The cross-section is a measure of the probability of an event, therefore it is not a real area with a well-defined boundary and it may not bear any close relationship with the physical size of atom cross-sectional area, which is approximately in the order of 10^{-16} cm^2. In electron microscopy, the cross-section of most processes is much smaller than the physical cross-section of atom. For example, the inner shell ionization cross-section is typically in the range of 10^{-22}~$10^{-24}cm^2$, and the total gas scattering cross-section studied in this paper, is at the order of 10^{-18}, 10^{-19} cm^2. So, it is sometimes referred to as the effective "size" which the atom or molecule presents as a target to the incident particle because it has the dimension of an area.

The full dimensionality of the cross-section for the scattering of electrons by atoms or molecules can be written as: Q (events/cm^3)/[(e-/cm^2)(atom/cm^3)] [Goldstein et al. 1992]. The cross-section is associated not only with electron scattering through a given angle but also with other types of reaction such as ionization, excitation, dissociation, molecular rotation, vibration, etc. Each possible interaction j is characterized by a cross-section σ_j, the sum of which is also the total cross-section σ_T [Danilatos 1988].

1.4.3.2 Rutherford and Mott Cross-section

From the macroscopic point of view, the majority of the incident electrons are considered as undergoing elastic scattering because the deflection from the inelastic scattering is so small (<<1°) that it can be ignored. So the elastic cross-section has always been the focus of study. Rutherford scattering is the elastic scattering produced by the Coulomb force. It happens when the incident electron is attracted by the positive charge in the nucleus, thus this scattering is often used to explore the shape of the nuclear charge,

The Rutherford elastic cross-section is widely used in various calculations because it gives analytical expression to compute θ, the angle of collision and λ, the distance between collisions (mean free path). There are several points to notice about the Rutherford scattering cross-section:

(a) It decreases rapidly with increasing angle θ;

(b) It becomes infinite at $\theta = 0$;

(c) This cross-section inversely proportional to E^2 (kinetic E) and

(d) It is proportional to $(Q_{target} * Q_{incident})^2$.

When the energy of the primary electrons is low or when the atomic number of the target is high, the Rutherford elastic cross-sections are inaccurate because this theory has been derived in the frame of the first Born approximation [Gauvin 1993]. In such case, Mott cross-section is more appropriate to use.

1.4.3.3 Mean Free Path (MFP)

An important parameter related with the cross-section is the Mean Free Path λ_i mentioned above. It can be defined as: the average distance traveled by a molecule between collisions. It can be shown that the Mean Free Path is given by Eq. 1.2 with given molecular diameter, d:

$$\lambda = \frac{1}{n\pi d^2\sqrt{2}} \qquad 1.2$$

As expected, there is an inverse relationship between the number density of the molecules (indicated by gas pressure) and the mean free path.

An electron with energy in the 5 – 2000 eV range passing through a solid can lose energy via a number of processes. Neglecting the minimal energy loss that occurs due to the excitation of phonons, there are three key processes: the electron-electron scattering processes, the excitation of a valence and excitation of Auger electrons. The net effect of these processes is that the Mean Free Path of an electron in a solid is strongly dependent on its kinetic energy.

A schematic plot of the variation in electron Mean Free Path as a function of electron kinetic energy is shown in Figure 1.13. This plot is usually referred to as the "universal" Mean Free Path and loosely holds for electrons traveling through a very wide range of materials. At very low kinetic energies the electron does not have enough energy to excite either of the listed processes, so its Mean Free Path is long. At high kinetic energies the electron spends less time passing through a solid, thus less likely to suffer from an energy loss and its Mean Free Path becomes quite long. The Mean Free Path passes through a minimum value between these two energy regions. The key process determining the minimum in the Mean Free Path is actually the energy loss due to plasmon excitation.

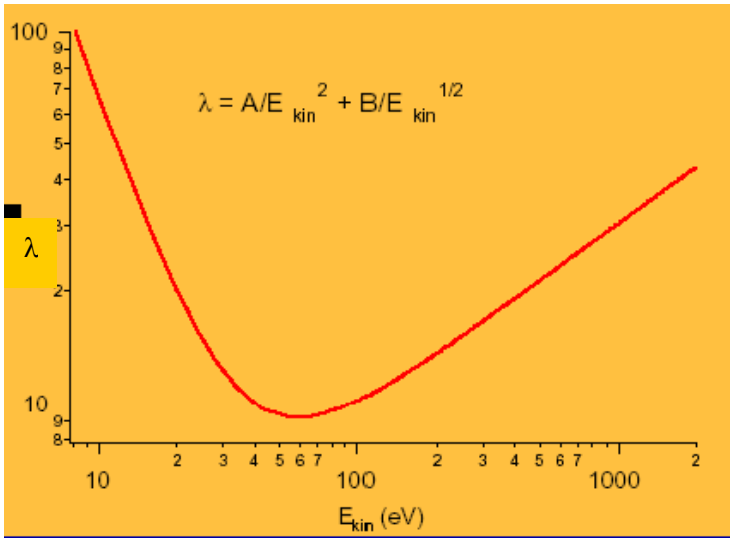


Figure 1.13 Mean Free Path and kinetic energy.

CHAPTER II
DIRECTLY MEASUREMENT OF THE ELECTRON BEAM SCATTERING

2.1 Introduction

As discussed in chapter I that the quality of the images of the samples, quality of the deposition, or etching during the micro processing, are all directly limited by electron scattering in the primary beam by the gas, therefore the scattering of electron which is not an issue in the conventional SEM, must be considered in the gaseous environmental SEM. The scattering effect was predicted by Danilatos [1988] originally and has been observed or measured by many researchers [Wight 1998, Gillen et al. 1998].

However, most of these experimental measurements and modeling are of limited value. There are many possible uncertainties associated with these second-hand-approaches because of the issues of X-rays production, absorption, geometry and collection efficiency etc [Wight 1999], which could result in the reduction on the accuracy of the study. Therefore the direct measurement of the distribution of the primary electron beam and scattered electron beam would be important if it was available. But the fact is that it is not easy to achieve because the extremely small size of the electron beam and the environment it usually works under. One method using phosphor imaging plates to directly measure the beam scattering has been introduced by Wight [1999].

We discuss here an alternative method in which a planar solar cell is used as an electron signal detector to determine the beam profile.

2.2 Introduction of P-N Junction Solar Cell

Solar cells were initially introduced as a global energy source without air pollution. Faced with ever-increasing demand, the earth's sources of non-renewable energy are not expected to last long. Among the many contenders vying to replace fossil fuels, photovoltaic solar cells offer many advantages, including needing little maintenance and being relatively "environmentally-friendly". A solar cell is a semiconductor device that converts light energy directly into electricity. For example, a typical 2x4cm silicon solar cell produces 0.45 volts and up to 0.275 amps or so of usable

current. The power generated by a cell is affected by the load resistance (of the circuit powered by the cell), intensity of sunlight, and temperature.

In its simplest form, the solar cell consists of a junction formed between n-type and p-type semiconductors, either of the same material (homo-junction) or different materials (hetero-junction). The band structure of the two differently doped sides with respect to their Fermi levels can be seen in Figure 2.1. When the two halves are brought together, the Fermi levels on either side are forced into coincidence, causing the valence and conduction bands to bend (Figure 2.2). These bent bands represent a built-in electric field over what is referred to as the depletion region.

When a photon with energy greater than the band gap of the semiconductor passes through the solar cell, it may be absorbed by the material. This absorption takes the form of a band-to-band electronic transition, so an electron/hole pair is produced. If these carriers can diffuse to the depletion region before they recombine, then they are separated by the electric field, causing one quantum of charge to flow through an external load. This is the origin of the solar cell's photocurrent, and is shown in Figure 2.3. Electrons impinging on the cell also produce current flow. A solar cell therefore is a useful detector of electron signals.

2.3 Experimental Method

In our electron beam profile measurements, light source planar p-n diode located inside the specimen chamber of the SEM is used as an electron signal detector. Its output is monitored by an amplifier in the SEM and the collected signal profile is displayed on the SEM display screen afterwards. The cell is mounted normal to the beam so that it presents an “active” area for detection just a few micrometers in width, but extending for several millimeters in width.

Before the electron beam strikes the solar cell, the signals appears on the profile will be just background noise. Once the electron beam starts scan through the positioned solar cell, the collected signals will increase dramatically due to the strong current created by the cell and reach to a peak value, than drop immediately as soon as the scanning beam passes by. For the case of conventional SEM, the electron beam probe is very sharp in the high vacuum, so the peak in the profile should be a narrow Gaussian line. For the scattered electron beam under gaseous environment, the peak is broadened due to the

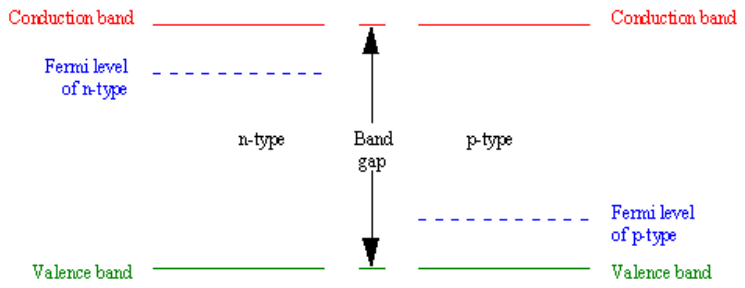


Figure 2.1 Band structures of differently doped semiconductors.

Source: http://www.dur.ac.uk/~dph0www5/solar.html

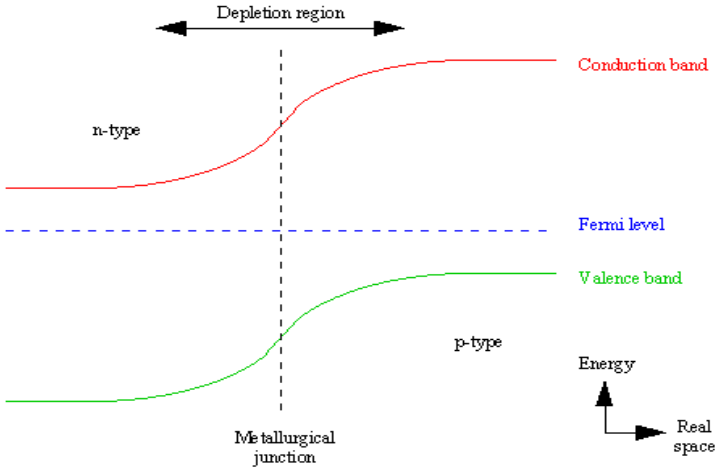


Figure 2.2 Band-bending structure of the hetero-junction.

Source: http://www.dur.ac.uk/~dph0www5/solar.html

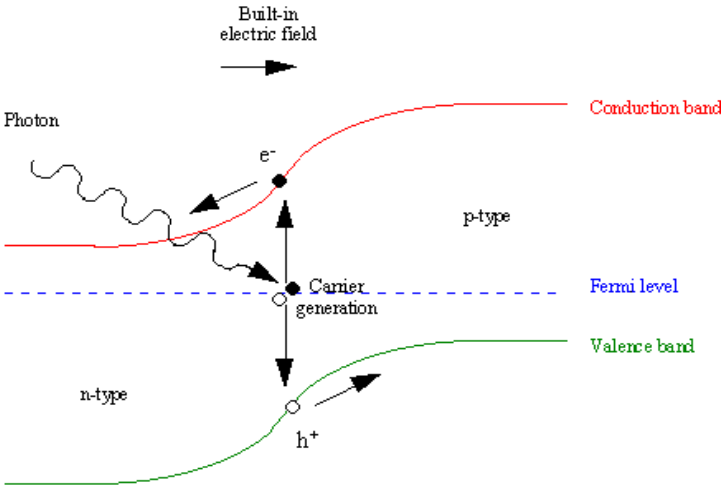


Figure 2.3 Principle of photovoltaic device.

Source: http://www.dur.ac.uk/~dph0www5/solar.html

scattering, and the broadening under various experimental variables, such as accelerating voltage of the electron beam gas pressure, gas composition beam gas path length etc that are the direct measurements of our interests.

The beam is scanned towards the diode as shown in Figure 2.4 to give the profile and at any position r of the beam center from the detector the collected signal is:

$$\text{Signal} = 2\int_{s=r}^{s=\infty} I(s)sd\theta \qquad 2.1$$

So I(r) can be recovered by deconvolution of this equation afterwards.

The signal is collected with the line scan parallel to the detector and the frame scan advancing at about 10μm/sec towards the diode. This averages the signals along the detector to make the collected signals smooth at both directions of parallel and vertical to the detector. At the same time it ensures that the profile is detected with long enough time not to be distorted by bandwidth limits in the amplifier.

2.4 Experimental Procedure

The experiments were performed in a Hitachi S-3500N VPSEM (Hitachi-high-Tech, Pleasanton, CA) at beam energies of 10, 15, 20, 25 and 30keV. A MKS Baratron® 626A Capacitance Manometer (MKS-Instruments, Andover, MA) was used to make pressure measurements, which were independent of the chemical composition of the gas. A Silicon solar cell, which could deliver approx 0.3 amps at 0.55VDC tested under full sunlight at noon on a clear day at 77ºF, was used as the signal detector.

On each side of the solar cell, a thin copper line was positioned to collect the current flow. One of the copper lines was connected with the amplifier of the VPSEM to produce a digital image formed by the detected electric current, using the Absorbed Electron (AE) mode in the VPSEM, and the other copper line was the ground return.

As we described, to assure the line scan parallel to the detector and the frame scan advancing towards the diode, the solar cell was mounted normal to the beam and the collected normal Secondary Electron (SE) image is as shown in Figure 2.5. The image produced by the solar cell, the AE image, is stored digitally as shown in Figure 2.6 and then analyzed using SCION image to produce the final line profile for deconvolution.

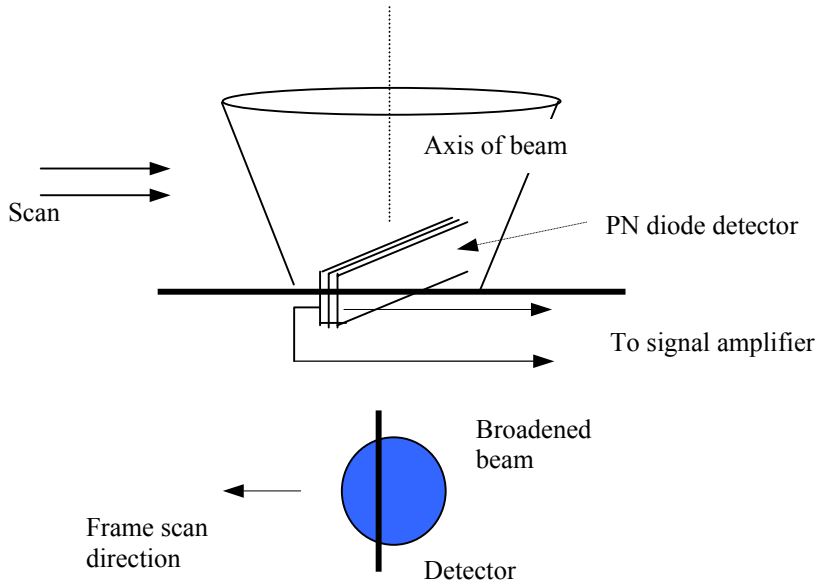


Figure 2.4 Schematic arrangement of measuring the beam profile in a SEM

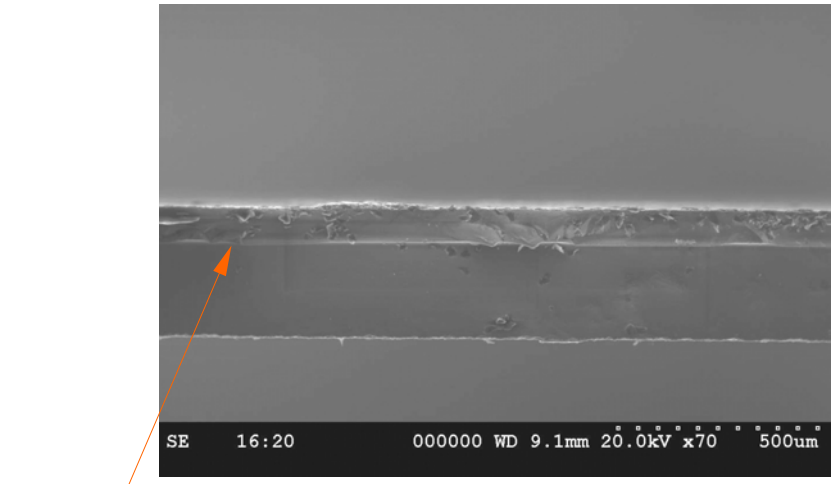


Figure 2.5 SE image of the positioned solar cell

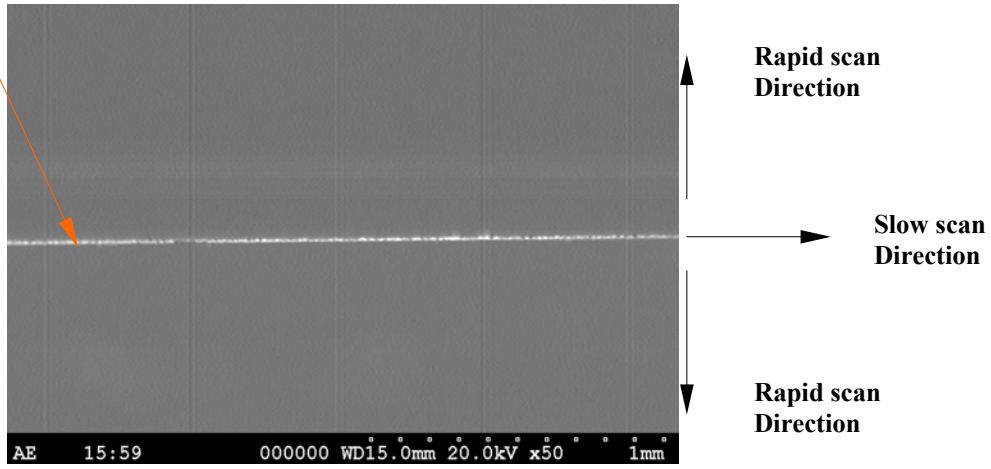


Figure 2.6 AE image detected by the solar cell

2.5 Experimental Results and Discussion

Data has been collected for several gases in the way described above.As shown in the raw data plotted in Figure 2.6, just as expected that before the electron beam strikes the solar cell, the signals are relative low because they were background noise only. Once the electron beam started to scan through the positioned solar cell, the collected signals increased dramatically and then dropped immediately when the scanning beam passed by.

The experimental profiles cover a wide range of intensity variation (Figure 2.7). There are two regions in the profile: an inner region where most of the electrons fall into and the signal here drop rapidly; and an outer skirt, though only small part of the electrons fall in this region, it could go as wide as ~100μm and where signal is relatively constant. These two regions correspond to inelastic (small angle) scattering and elastic scattering (relatively large angle) respectively.

2.6 Summary

The measured profiles use the planar p-n junction gives us an overall look at the electron beam spreading, including the oversize and shape of the profile. However it does not provide useful information about the center of the electron beam, which is the area of more interest in our study.

Considering the efficiency of these measurements, we developed another method to evaluate the electron beam scattering, which is to develop a Monte Carlo simulation of the beam scattering profile with experimentally measured data on the total gas scattering cross-sections, which could provide more detailed electron scattering information of the relative smaller scattering angle area around the beam center.

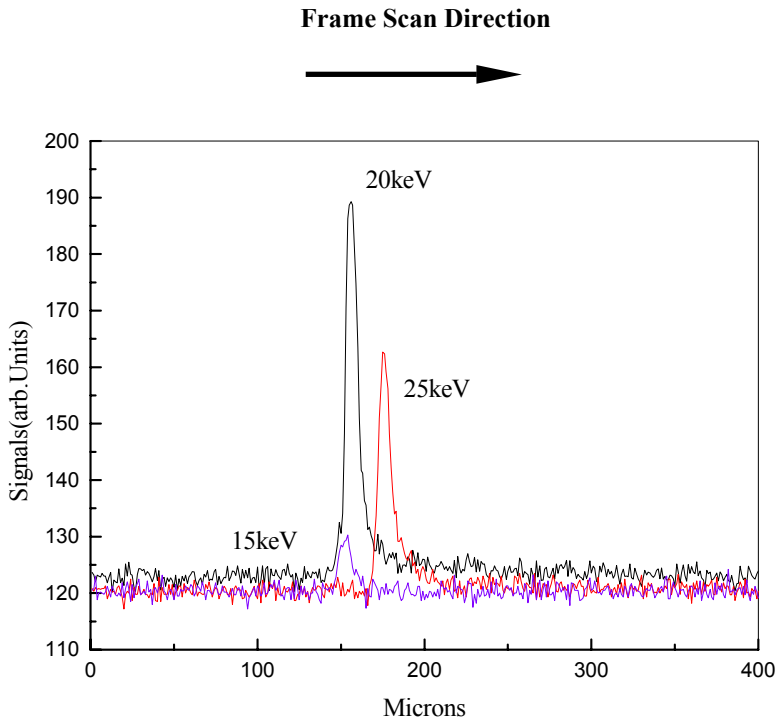


Figure 2.7 Raw profile data collected at 15, 20, 25keV.

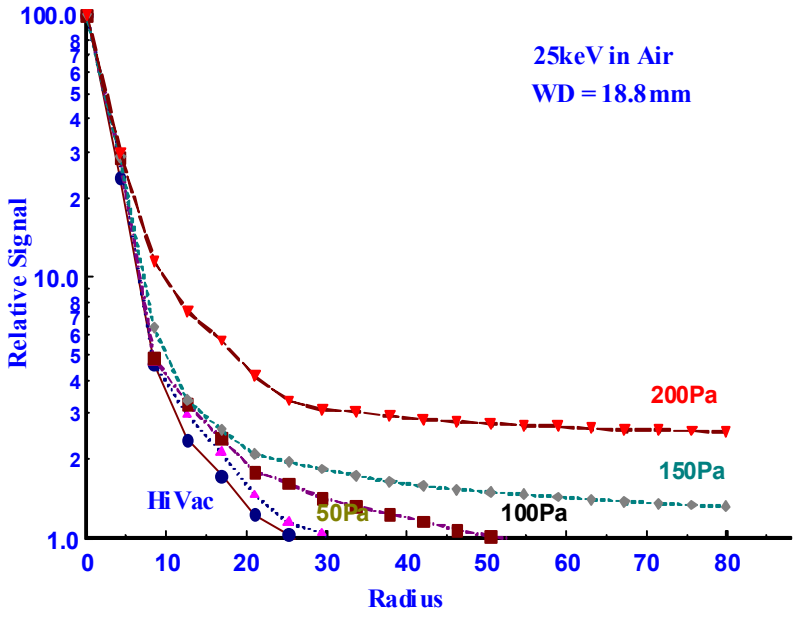


Figure 2.8 Scattered beam profiles in Air at E = 25keV after deconvolution.

CHAPTER III
MEASUREMENT OF TOTAL GAS SCATTERING CROSS-SECTION

3.1 Introduction

The total gas scattering cross-sections data is one of the essential information required for developing a Monte Carlo simulation of the beam scattering. However there seems considerable difficulty in establishing a universal theory of scattering cross-sections for all gases that can be confirmed by experiment. Relatively few total gas scattering cross-sections are available for the conditions of gas pressure, and electron beam energy that are of interest in the electron microscopy field. Cross-section values are not easy to compute because the vibrational modes of the gas molecules add an additional contribution to the value of the scattering cross-section, and they are also difficult to predict unless the atomicity (i.e. effective atom cluster size [Ditmire 1997]) of the molecule of gas is known. Since the experimental data available on cross-sections are definitely inadequate and because there is also insufficient experimental verification for the theoretically calculated cross-sections in current use, systematic experimental measurements of the total gas scattering cross-sections presented are necessary.

In our project, the total gas scattering cross-section was experimentally measured using the technique of Gauvin [Gauvin et al. 1999]. This method depends on an observation of the variation of the fluorescent X-ray intensity excited by the electron beam with variable gas pressure from a small target. The advantage of this technique is that the variation of X-ray intensity with pressure will be due only to the decrease of the on-axis intensity of the unscattered beam with pressure, since the scattered part of the beam goes into the skirt region of the beam and hence misses the particle, so reducing the signal collected by X-ray detector. The effect caused by any ions generated from secondary electrons on the current measuring by the Faraday cup is eliminated here since it is only the characteristic X-ray intensity of the specified spot on specimen that is measured.

3.2 Experimental Method

A stationary beam of electrons is focused on to a small target (~25μm in diameter) as shown in Figure 3.1. The X-ray signal produced from the object is then

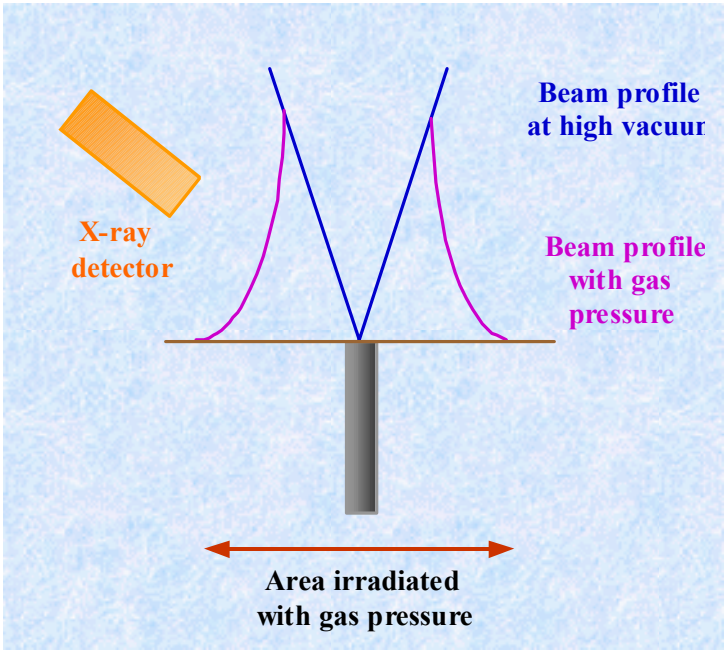


Figure 3.1 Schematic of the experimental technique.

measured as a function of the gas pressure. As the pressure increases electrons are scattered into the skirt and so miss the object and the X-ray signal falls.

The total scattering cross-section of gas can then be calculated by an equation derived from the expected Poisson distribution of the scattered electrons and the Gas Law as [Gauvin et al. 2000]:

$$\ln(I) = -\frac{D\sigma_T}{RT}P + \ln(I_0) \qquad 3.1$$

where I is the measured X-ray intensity at a given pressure P, σ_T is the total elastic cross-section of the gas at certain energy of electron beam, D is the gas path length (i.e. the average distance traveled by an incident electron from the position where it leaves the high vacuum region of the VPSEM to the point where it reaches the sample surface), R is the perfect gas constant and T is the temperature in degree Kelvin. With the slope, α obtained from the linear relationship between $\log_e(I)$ and P identified by Eq.3.1, the total scattering cross-section can then be easily deduced as indicated in Eq.3.2:

$$\sigma_T = -\frac{\alpha RT}{D} \qquad 3.2$$

The cross-section determined in this way will include all elastic and inelastic events which scatter the incident electron through and angle $\phi > \rho/D$, where ρ is the diameter of the target, here ϕ is about 2 milliradians.

3.3 Experimental Procedure

The experiments were performed in a Hitachi S-3500N VPSEM (Hitachi-high-Tech, Pleasanton, CA) as indicated in Figure 3.2, with a GRESHAM EDS detector (GRESHAM-Scientific-Instrument, Marlow, Buckinghamshire, UK) at beam energies of 10, 15, 20, 25 and 30keV. A MKS Baratron® 626A Capacitance Manometer (MKS-Instruments, Andover, MA) was used to make pressure measurements, which were independent of the composition of the gas.



Figure 3.2 Experimental equipment (VPSEM, EDS, Manometer).

In order to optimize the collection of the X-ray emission the specimen was held at the standard X-ray position corresponding to a gas path length of 12 mm, and the magnification was x18K. The X-ray intensity was obtained by collecting the X-ray signals emitted by the surface of a fine aluminum wire of 25 μm diameter inlaid in epoxy resin (Figure 3.3). To avoid charging build up resulting from the use of a nonconductive resin, the specimen was coated with a thin layer of gold-palladium. The selected fluorescent X-ray peak in this experiment was Al kα whose characteristic energy is 1.5 keV and the counting time (i.e. live time) was 300 seconds. For the chosen beam energy data was then recorded as the pressure was raised from below 1 Pa to its maximum value, typically 270Pa. A second run of data was recorded as the pressure was reduced back to 1Pa. This was done to ensure efficient mixing of the gas of interest as discussed below. The gas was introduced into the chamber through the computer controlled inlet needle valve. A small container of the gas of interest, at a pressure just slightly above atmospheric, was connected directly to the intake nozzle by a short piece of tubing.

3.4 Experimental Results

3.4.1 Linear Relationship of Ln (I) and P

As demonstrated above Gauvin's technique suggests a linear relationship variation of ln (I_p/I_0) with Pressure, and as seen in Figure 3.4 through Figure 3.8, this prediction is experimentally obeyed very well over a wide range of gas species and incident beam energies, which indicates that the established basic model is correct. These plots shown clearly illustrate how different gases scatter electrons by different amounts. The data points plotted are the average of the values obtained as the pressure is first increased to 300 Pa and then decreased back to 0 Pa.

3.4.2 Calculated Total Scattering Cross-sections

From these plots, the total gas scattering cross-section can be easily derived from the slope of the data line at each energy as discussed in Eq 3.1, 3.2.

For multiple sets of raw data obtained in different time period for gases, statistic models were fit to all sets of data points to test the variablilities over different trials:

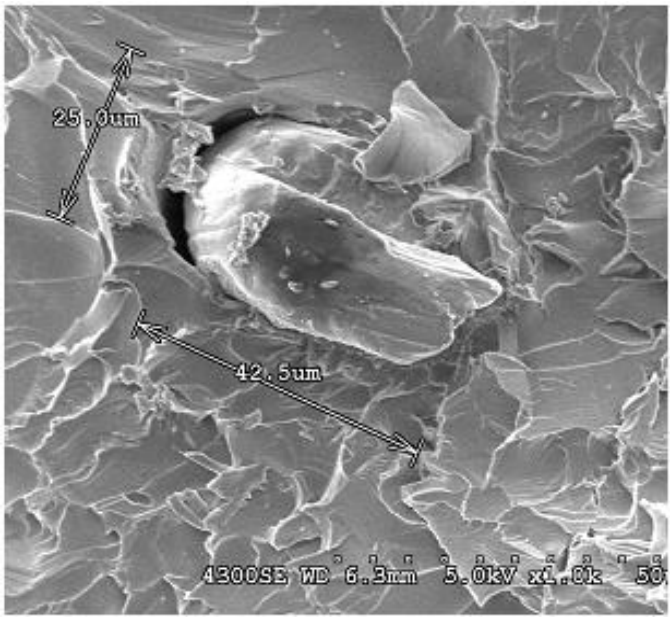


Figure 3.3 SEM image of the Al wire cross-section.

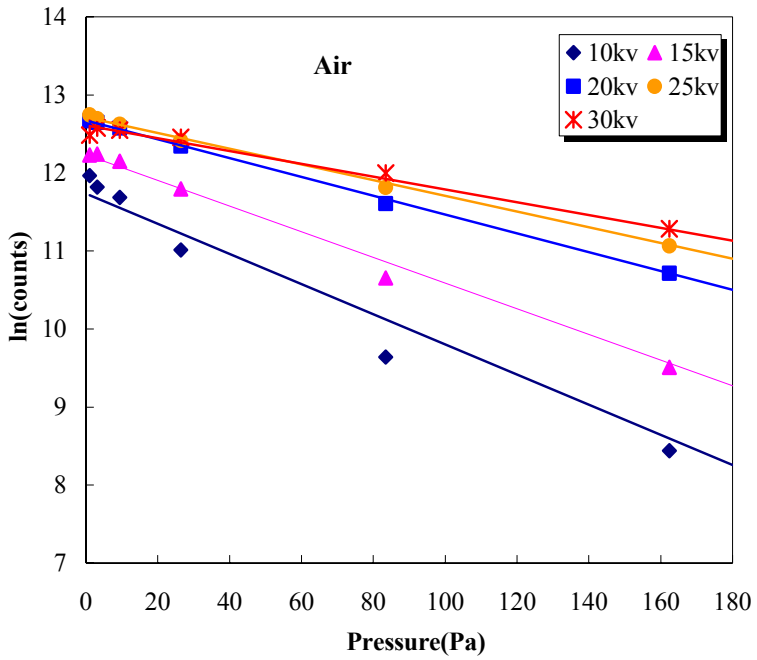


Figure 3.4 Linear relationship of ln (I) and P for Air.

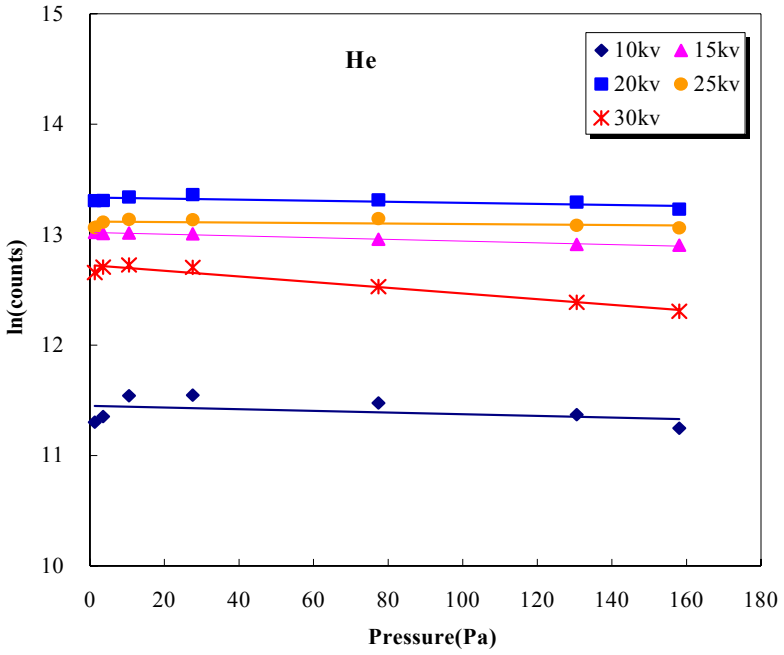


Figure 3.5 Linear relationship of ln (I) and P for Helium.

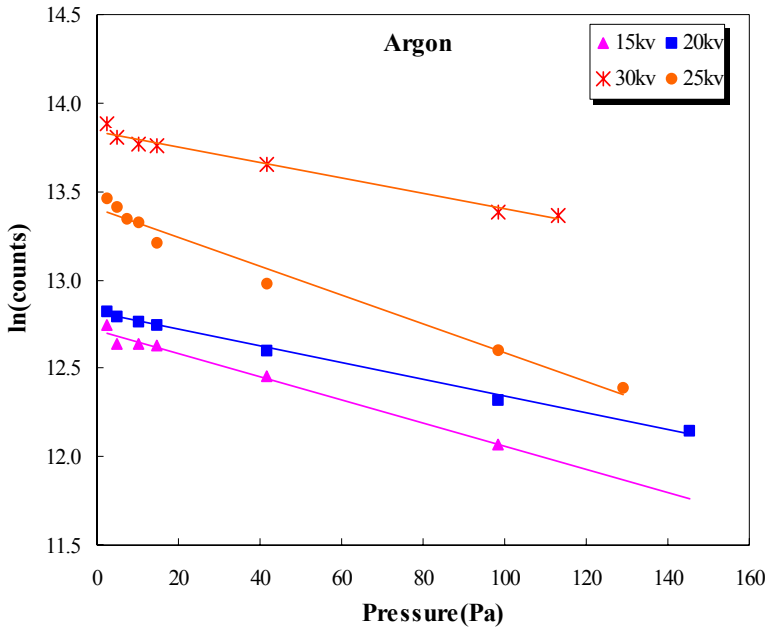


Figure 3.6 Linear relationship of ln (I) and P for Argon.

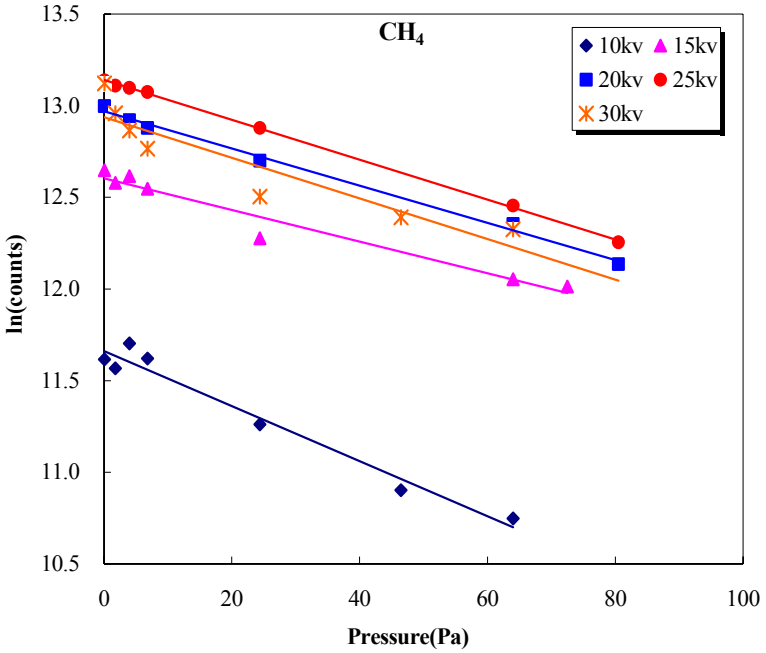


Figure 3.7 Linear relationship of ln (I) and P for Methane.

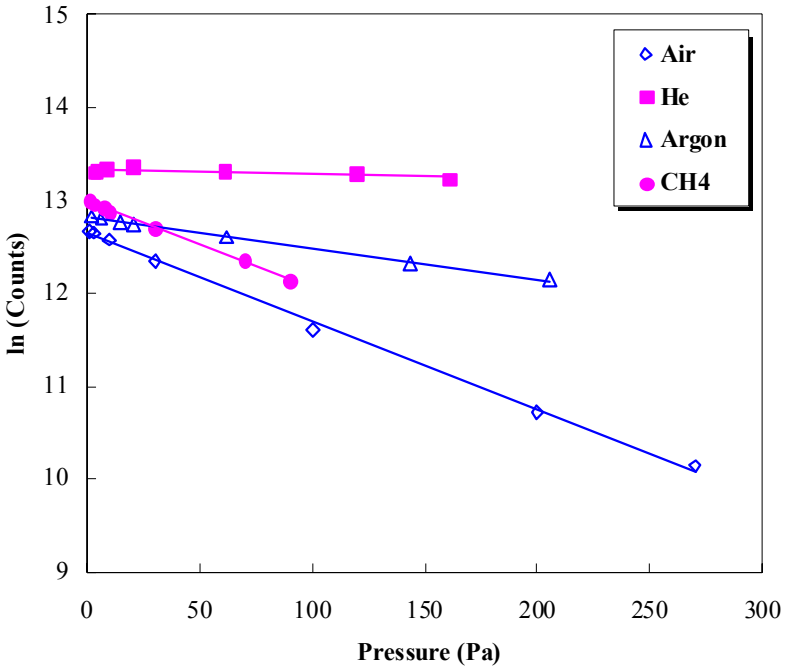


Figure 3.8 Linear relationship of ln (I) and P for gases at 15keV.

- If the factor Pressure*Trial is statistically nonsignificant at level of 0.01 in the tests, it suggests that the variability due to different trials are nonsignificant. Therefore the final regression line for that beam energy was deduced based on all sets of data without the Pressure*Trial term in the model. With the slope of the regression line, the cross-section (σ) value with its standard error (SE) can be easily calculated.
- If factor Pressure*Trial is statistically significant at level of 0.01, it means that the variability caused by different trials can not be ignored. A model was constructed considering the Trial as random effect, and the regression line was fitted to the model using REML (REstricted or REsidual Maximum Likelihood) [Montgomery, 2000] approach. With the slope deduced from the regression line, the cross-section (σ) value with its standard error (SE) was then calculated.

Based on the method described above, the obtained total gas scattering cross-sections of air with the theoretical Mott's cross-sections of air are listed in Table 3.1. For higher beam energy, the stronger linear relationship between the ln (I) and air pressure, which result in larger scattering cross-section. The reason is at higher beam energy, electron beam is less likely scattered, so more emitted Alkα signals can be collected. The difference between the experimental calculated cross-section of air and Mott's cross-sections for air is also noticeable. One possible reason suggested by the data is that in this pressure regime most gas molecules are aggregated in clusters. Another reason is that Mott's cross-section only accounts for a part of the total scattering event - the elastic scattering.

The calculated total scattering cross-sections of other investigated gases are also tabulated below (Table 3.2) in units of cm^2/atom. As anticipated helium scatters the least strongly (i.e. has the lowest cross-section) while air scatters the most strongly (i.e. highest cross-section), the difference being about a factor of 10 times. As the beam energy rises the scattering cross-section would be expected to fall, as is observed for air and helium. The somewhat anomalous behavior of the argon and methane data, in which the cross-section between 20keV and 30keV remain essentially constant with beam energy, may be the result of less than perfect mixing of the gas in the specimen chamber, or of statistical or of uncorrected errors in the procedure.

Table 3.1 Comparison between the calculated total gas scattering cross-sections of air and the Mott's cross-sections of air

Voltage (keV)	GPL (mm)	α	σ (cm^2/atom)	SE	σ (cm^2/atom) [Mott]
10	12	0.01596	5.51E-17	2.68E-18	6.79E-18
15	12	0.01421	4.90E-17	4.37E-18	4.61E-18
20	12	0.01357	4.68E-17	8.51E-18	3.49E-18
25	12	0.01341	4.63E-17	7.15E-18	2.82E-18
30	12	0.01298	4.48E-17	7.71E-18	2.37E-18

Table 3. 2 Experimental Calculated Total Scattering Cross-section

Beam Energy (keV)	Air		He		Argon		CH_4	
	σ (cm^2/atom)	SE	σ (cm^2/atom)	SE	σ (cm^2/atom)	SE	σ (cm^2/atom)	SE
10	5.51E-17	2.68E-18	2.45E-18	6.38E-19	-	-	5.18E-17	4.18E-18
15	4.90E-17	4.37E-18	2.00E-18	1.48E-19	2.24E-17	1.21E-18	2.97E-17	2.84E-18
20	4.68E-17	8.51E-18	1.31E-18	4.62E-19	1.62E-17	6.00E-19	3.49E-17	1.13E-18
25	4.63E-17	7.15E-18	7.83E-19	3.04E-19	2.80E-17	1.62E-18	3.76E-17	3.83E-19
30	4.48E-17	7.71E-18	8.86E-18	8.49E-19	1.59E-17	1.17E-18	3.69E-17	1.60E-18

3.5 Discussion of Errors in the Procedure

Before comparing the experimental total scattering cross-sections with theoretical values, there are several key factors in this experimental procedure which need to be discussed, first to assess the accuracy and precision of this work: the measurement of gas pressure, the determination of the gas path length (GPL), and the alteration of the gas temperatures inside the specimen chamber.

3.5.1 Gas Pressure Measurement in the VPSEM

In an environmental or VPSEM, the pressure is controlled by a computer operated leak valve and a suitable feedback circuit monitoring the pressure read by a Pirani gauge. Typically this leads to a condition in which the pressure cycles slowly with time about the nominal value as the valve opens and closes, and results in the difficulty of the correct determination of the gas pressure. Furthermore, on our instrument the gauge is positioned very close to the inlet valve and therefore reads a pressure which may not be truly representative of the true chamber vacuum. Finally, the reading of the Pirani gauge is strongly dependent on the chemical composition of the gas to what it is being exposed [Bigelow 1994].

To overcome the limitations of the Pirani gauge supplied with the VPSEM, a MKS Baratron® 626A Capacitance Manometer (with 0.25% accuracy) was installed in the S-3500N VPSEM as indicated in Figure 3.9. The Capacitance Manometer transducer is an active sensor, which makes gas composition independent pressure measurements and provides a real-time digital readout. Pressure is determined by measuring the change in capacitance between the diaphragm and an adjacent dual electrode. The differential capacitance signal is converted into a useable output by signal conditioning circuitry. The type 626A Absolute Pressure Transducer (~0.25% accuracy) applied in our experiments could give reliable and repeatable pressure measurements in the range from 10^5 Pa to as low as 10^{-3}pa.

With the employment of the Capacitance Manometer, much more accurate and reliable chamber gas pressure reading could be obtained both because of the gas independence of the measurements, and because of the position of the gauge inside the specimen chamber. This step enhances the accuracy of the measurement of the total gas

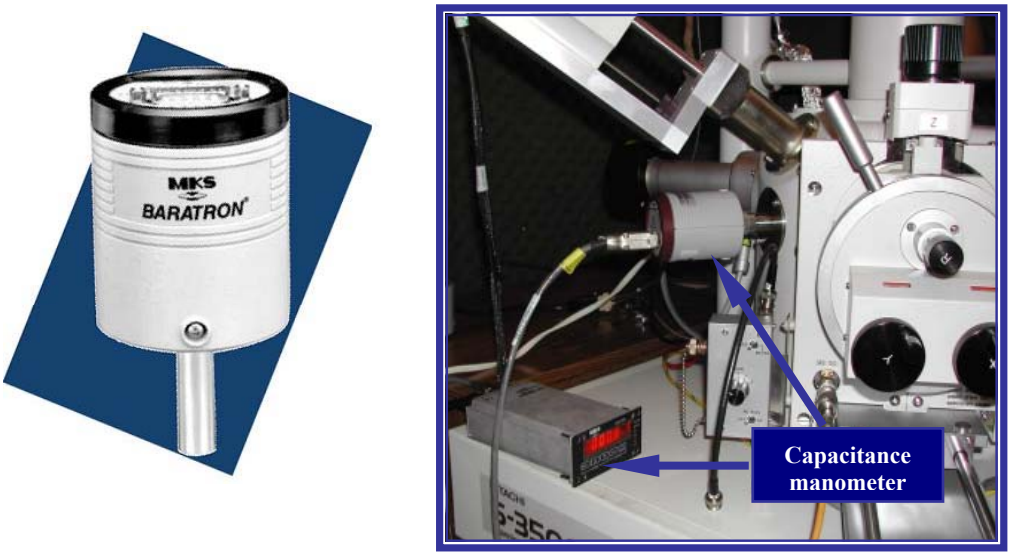


Figure 3.9 MKS Baratron® 626A capacitance manometer.

scattering cross-section. For a given pressure setting the observed time varying fluctuation in pressure was typically a few percent.

The pressures of the gases of interest were measured by the manometer capacitance, and all the pressure readings along with the nominal pressure readings from the Pirani gauge were plotted in Figure 3.10. The deviations of the pressure readings from these two gauges are obvious, even for laboratory air.

3.5.2 Confirmation of the Gas Path Length

The calculation of the scattering cross-section also depends on the value of the Gas Path Length (GPL), which is the distance through which the incident beam travels between the Pressure Limiting Aperture (PLA) and the specimen surface. The nominal working distance was considered to be the GPL in the cross-section calculation, but the actual GPL may be longer due to the fact that some gases may enter the upper column through the PLA.

A test was therefore conducted to confirm the correct effective value of the GPL. Two successive experimental runs were carried out under identical conditions but with the sample shied by 1mm to change the GPL by a known amount (Figure 3.11). An application of Eq.3.1 and 3.2 give a value for D which is consistent with the nominal value of D = 12 mm. This indicates that the high pressure region through which the beam passes is confined to the area beneath the pressure limiting aperture which is positioned at the bottom surface of the lens, and that there is no significant penetration of the chamber gas above the PLA for the pressures used in these experiments [Gauvin et al. 2002]. It is therefore correct to equate the working distance and GPL in this case.

3.5.3 Confirmation of the Temperature Variation

The computed value of σ_T depends directly on the assumed temperature of the gas. The actual temperature of the gas inside the chamber would be expected to be significantly lower than its temperature outside the chamber because the expansion of the gas into the low vacuum of the SEM chamber causes cooling.

A sensitive thermocouple was installed on the VPSEM to test the temperature variation and positioned close to the inlet gas jet in the specimen chamber. During the

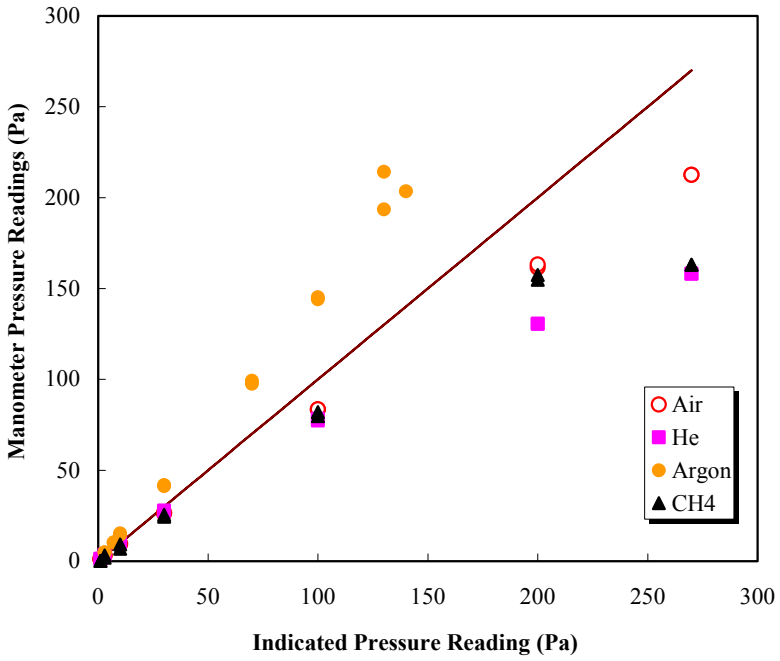


Figure 3.10 Pressure readings by capacitance manometer and Pirani gauge.

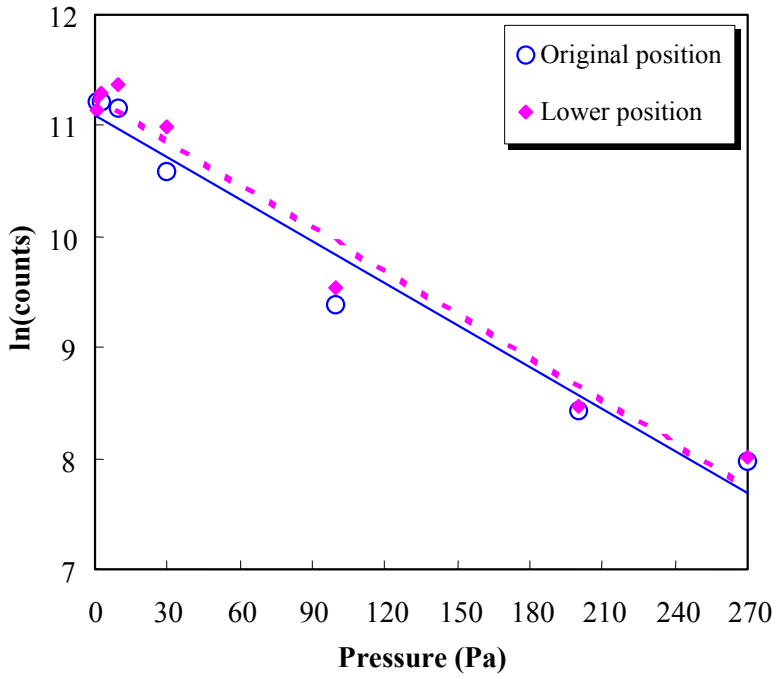


Figure 3.11 Comparison of the collected X-ray signals at two GPLs.

pumping down process, the temperature did initially drop from 26.3° C to 23.0° C within several seconds, but as the gas pressure stabilized at the desired level, the gas temperature

recovered almost to the starting value, with a very small deviation of around 0.1° C, suggesting that the gas rapidly achieves thermal equilibrium by contact with the chamber walls. Therefore, based on our measurement of the temperature variation, on average, the gas temperature is considered as constant and equal to normal room temperature during the whole experimental process.

3.5.4 Possible Noise Signals from the Background

The X-ray intensity is expected to decrease with the increasing of the gas pressure, as more and more electrons are scattered outside the beam, resulting in a decrease in the collected emission signals from the Al wire. However, from the raw data we can see that the tendency of the signal variation is not exactly as we expected, there are some spikes in the initial part of the curve instead of smooth decreasing curve. One of the possible reasons is probably rising from the background noises.

Based on this observation, the background signals were recorded while the selected X-ray signals were collecting at each pressure level. Since the characteristic energy of Alkα is 1.5keV, so the energy range of the recorded background of the Alkα peak in the spectrum was selected as 2keV to 6keV. The experiments processed under 15keV and 20keV are plotted in Figure 3.12.

From the recorded background signals we can see that they are exhibiting the same variation as the collected signals during most of the processing time, decreasing with the increase of the gas pressure and some fluctuations appear at lower gas pressures range. So, obviously the background signals are not the reason for the fluctuations in the Al kα signal collection. However the constant background signals during the measurement, which may be related with the variation of the emission current of the electron probe, could result some measuring errors in the whole experimental procedure.

Since it is the natural logarithm of the X-ray intensity that we are concerning about right now, the deviations at the lower pressure range are presently considered as acceptable factor for our experiments as long as they won't affect the linear relationship

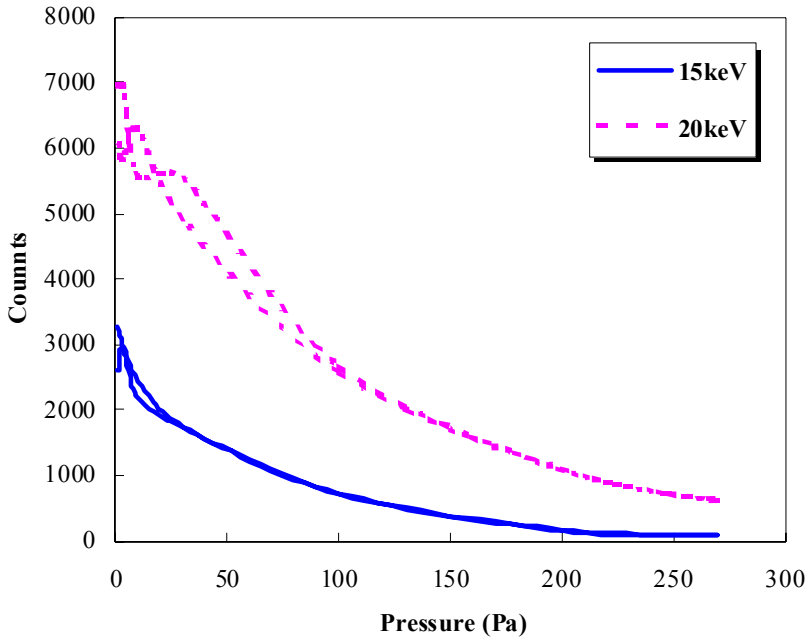


Figure 3.12 Background signals under 15keV and 20keV.

between the $\log_e$(Intensity) and gas pressure. The background signal factor is therefore ignored presently and it will be considered in our further researches.

3.6 Experimental Results Discussion

So far the experimental data has been collected for four gases: He, Air, Methane, and Argon. Excellent agreement is found with values computed from the theory of Jost and Kessler [Danilatos 1988] over the energy range of 10-30keV used in the experiments. The experimentally obtained total scattering cross-section for Helium is plotted and compared with theoretical values in Figure 3.13, and the cross-sections from experiment and theory agree very well. There is some deviation at lower beam energies, which may due to the omission from the theoretical model of some possible inelastic contributions to the cross-section.

In the pressure range used for this work, many gases are believed to be molecular rather than atomic in nature. The so-called "van der Waals bounded complex" was discovered in 1965 are atomic clusters that can be simply created by the expansion of a jet of gas into vacuum. The cooling associated with the gas's adiabatic expansion causes the gas to supersaturate and the atoms nucleate into clusters. These macromolecules systems have caused much attention because they appear to bridge the gap between a molecular and a bulk solid state form of matter.

How large does an assemblage of single atoms have to become before it begins to take on the properties of a bulk solid? The answer depends on the characteristics of the studied material (e.g., Ar clusters: > 2000 atoms, Li clusters: > 130 atoms and V clusters: > 30). Atoms and Molecules in clusters behave in a different manner to those contained in liquid or solid substances. In spite of its size, behaviors of cluster do not simply evolve continuously from those of an atomic to macroscopic scale [Ditmire 1997]. So, the total scattering cross-section for a molecule may be not just the sum of the atomic cross-section. Additional interactions with the incident electron beam are very possible due to binding of atoms in molecules, considering the outer region is primarily responsible for scattering at the smallest angles [Danilatos 1988]. Both the theoretical molecular cross-section and atomic cross-section for Nitrogen were plotted in Figure 3.14 and it clearly verifies that the molecular cross-section of N is larger than just simply twice the atomic cross-section value of N. The differences increase at the lower beam energy range.

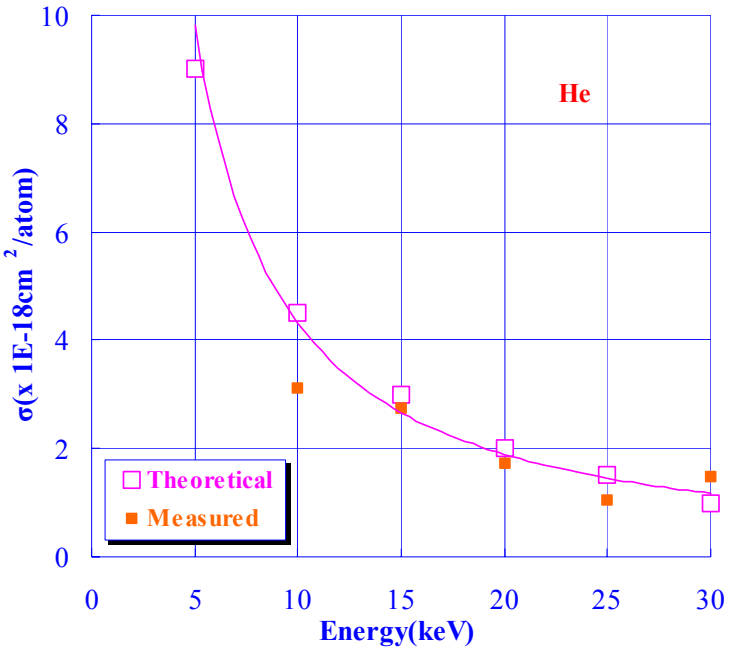


Figure 3.13 Comparison of theoretical and experimental cross-section for atomic Helium.

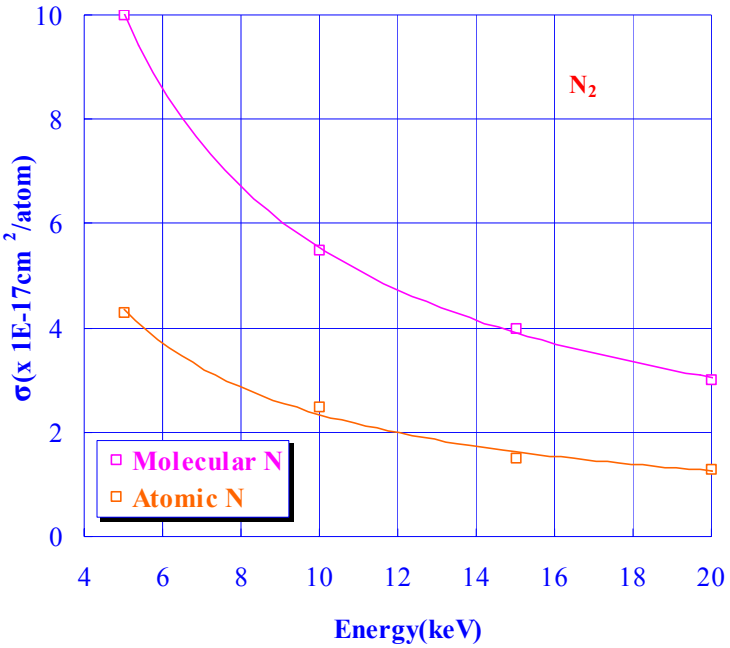


Figure 3.14 Theoretical cross-section for atomic and molecular Nitrogen.

Since the most commonly used chamber gas is 'laboratory' air, the collected experimental data of total scattering cross-section for air is compared with theoretical total cross-sections of atomic N, molecular N_2, molecular O_2 (the curve for O_2 lies just below that of N_2 and is not shown for clarity) and water vapor in Figure 3.15. As demonstrated by the curves, the measured total scattering cross-section for air tracks closely with that for molecular rather than atomic Nitrogen. It is higher than the value for water vapor (at Room Temperature and Pressure) as expected since the partial pressure of the water vapor is below the saturation value.

3.7 Summary

The experimental total scattering cross-section data obtained in these experiments is of great interest. It shows the excellent agreement between experimental values and theoretical estimates of the total gas scattering cross-section. The new method of the measurement of the gas scattering cross-section has been validated by this data and the predicted linear relationship between $\log_e(I_p/I_0)$ and gas pressure has also been confirmed.

On the basis of the available evidence, gases tend to be molecular rather than atomic in nature in the pressure range used in the performed experiments. During the experimental procedure, the temperature variation could be ignored in our calculation in average and it is also reliable to equate the working distance of the VPSEM to the gas path length (GPL) in calculations of the scattering cross-section.

In our future work the total cross-sections of more complex gases, such as XeF_2, $W(CO)_6$ etc. metallic gases selectively used for etching and depositing will be measured and a more precisely controlled method of gas induction, for example, a localized small gas jet with needle valve to position gases to just the area around specimen, will be tested and used in further experiments. In next of this work, the experimentally collected gas scattering cross-section data will be inserted into Monte Carlo simulation program to predict the spatial distribution of the electron beam scattering under given beam energy.

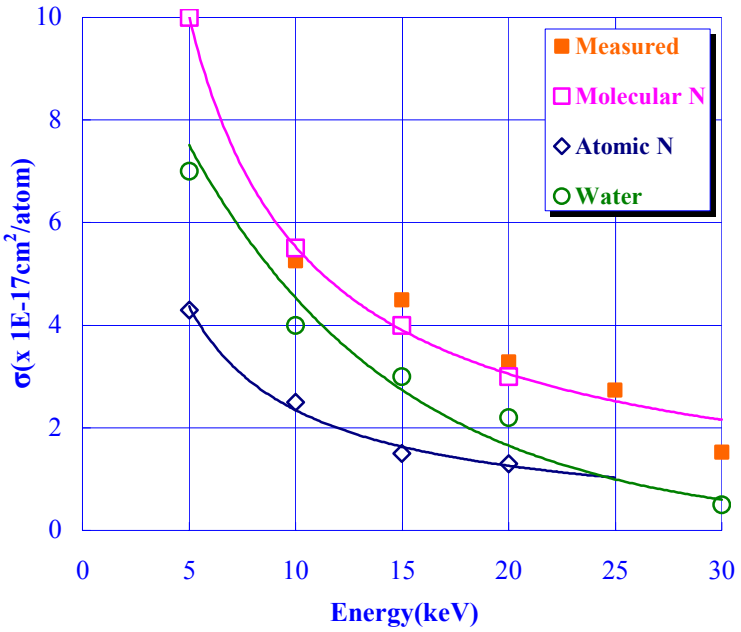


Figure 3.15 Experimental cross-section for air compared to its components.

CHAPTER IV
MONTE CARLO SIMULATION OF THE ELECTRON BEAM SCATTERING

4.1 Introduction of Monte Carlo simulation

4.1.1 Background Introduction

Monte Carlo simulation as it is often called should more correctly be titled Monte Carlo sampling since it uses random numbers to sample either experimental or theoretical data. The first published example of the use of random numbers to solve problem is that of Buffon, who-in his 1777 volume Essai d' Arithmetique Morale-describe an experiment in which needles with equal length were thrown randomly over a sheet marked with parallel lines. Amazingly, by counting the number of intersections between lines and needles, Buffon was able to derive a value for π. Subsequently many other mathematicians and statisticians followed Buffon's lead and started to use random numbers as a way of testing theories and results. For example, in the early twentieth century, radioactive decay or the transmissions of cosmic rays through barriers all have been investigated by random numbers [Joy 1995].

Monte Carlo sampling techniques was known by its extensively application during the Manhattan project by Von Neumann and Stan Ulam, who refined this investigation as " Russian roulette" and "splitting" methods at that time. They made use of both random-number sampling and game-playing situations involving random numbers as a way of studying physical processes as diverse as neutron diffusion and the probability of a missile striking a flying aircraft. But Enrico Fermi was actually the first scientist who had independently developed the Monte Carlo method in the early 1930's when he was studying the moderation of neutrons in Rome. Then during the hiatus in the ENIAC (first electronic computer) operation in 1947, he built an instrument called the FERMIAC to develop neutron genealogies in two dimensions by generating the site of the " next collision". Each generation was based on a choice of parameters that characterized the particular material being traversed. About 1948 Fermi, Metropolis, and Ulam obtained Monte Carlo estimates for the eigenvalues of Schrodinger equation [Metropolis 1987]. Nowadays the Monte Carlo method has a wide range of applications, from the simulation

of bit error rates in telecommunications to evaluate definite integrals, from the simulation of natural phenomena to the simulation of experimental apparatus etc.

Monte Carlo method is a statistical simulation of a probability density function based on sequences of random numbers. It has two basic features, one is simple structure of the computational algorithm and the other is the error satisfies the proportionality:

$$\varepsilon \propto \frac{\sigma}{\sqrt{N}} \qquad 4.1$$

The use of random sampling to solve a mathematical problem can be characterized as follows. A game of chance is played in which the probability of success P is a number whose value is desired. If the game is played N times with r wins then r/N is an estimate of P. A modern version of the "π"-calculation could be demonstrated as following (Figure 4.1).

A circle with radius of r is drawn enclosed in a square and we shoot darts at the square randomly (without aiming) *N* times. Then we have a numerical relation between the darts and the areas:

$$\frac{\#\,\text{darts hitting inside circle}}{\#\,\text{darts hitting inside square}} = \frac{\text{area of circle}}{\text{area of square}} \qquad 4.2$$

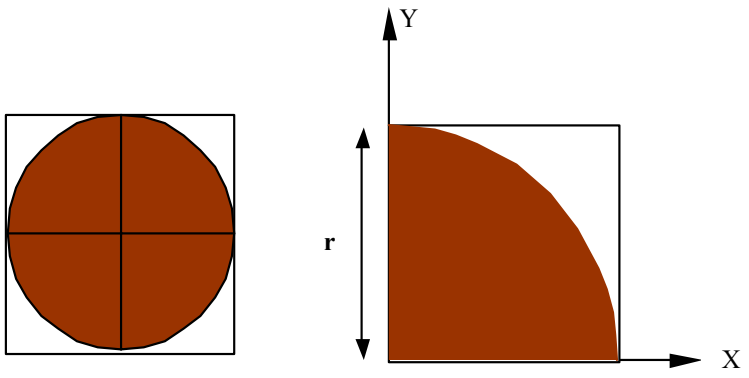


Figure 4.1 Monte Carlo Calculation of π.

Considering the geometry, we could have

$$\frac{\#\,\text{darts hitting inside circle}}{\#\,\text{darts hitting inside square}} = \frac{\pi r^2 / 4}{r^2} \qquad 4.3$$

Finally we could get π from equation 4.3:

$$\pi = 4\frac{\#\,\text{darts hitting inside circle}}{\#\,\text{darts hitting inside square}} \qquad 4.4$$

4.1.2 Random Number Sampling

The "random numbers" is the core concept of the Monte Carlo method. However "there is no such a thing as a random number", rather we speak of a sequence of independent random numbers with a specified distribution, which means loosely that each number was obtained merely by chance, independent of other numbers of the sequence and each number has a specified probability of falling in any given range of values. So the implication of a random number is that any number within a specified range (usually 0 to 1) has an equal probability (i.e. 1 in 10) of occurring. The "random numbers" are just pseudo-random. They only appear to be random because there is no simple or apparent connection among a sequence of these values, but actually are determined by certain mathematical algorithms.

Thus to take a simple and relevant example, consider an electron that can be scattered elastically or inelastically the probability (p_e for elastic scattering and p_{ie} for inelastic scattering) of either scattering occurrence being determined by its total cross-section. A choice could be made between the two alternatives by picking a random number RND ($0 < RND < 1$) and specifying that if $RND \leq p_e$ then an elastic event occurs, otherwise an inelastic event occurs.

4.2 Monte Carlo Simulation of Electron Trajectories in a Solid

It was not until 1955 that the Monte Carlo method was successfully employed for charged particles by Herbbard and Wilson [Hebbard et al. 1955]. In this applied field, the

Monte Carlo technique using random numbers as a means of predicting the magnitude of various events and as a way for selecting between possible scattering options [Joy 1995]. Before ultimately losing its energy or escaping from the specimen, each incident electron may undergo hundreds or thousands of separate scattering events, distributed between elastic and a variety of inelastic processes. It is necessary to be able to describe in detail the processes, which produced that data in the first place, but this is not a simple task because the interaction between the electron beam with a solid is highly complex. The Monte Carlo method was therefore developed for the quantitatively study of the electron microscopy technique to correctly interpret images or spectra.

4.2.1 Basic Principle

The Monte Carlo technique, as applied in the electron microscopy field, attempts to describe the trajectory which takes the electron through the solid. Although no individual trajectory produced by the simulation will represent a real trajectory, if the physics of the processes encountered (Figure 4.2) by the electron are properly modeled then predictions based on a large number of trajectories will accurately describe effects which can be experimentally observed. In order to make these calculation possible, two basic pieces of information, the scattering angle, through which the electron is scattered and the average step length between two successive scattering events given particular incident energy are required [Joy, 1995].

The basic principle of this application [Goldstein et al., 1992] is that the step length of the basic repetitive step in such a calculation is usually set as some fraction of the Mean Free Path (i.e. the average distance traversed by a molecule between collisions, as introduced before, it is a key parameter related with the electron scattering study and the Mean Free Path (MFP) of an electron in a solid is strongly dependent on its kinetic energy) for elastic scattering ("single scattering Monte Carlo") or a multiple scattering ("multiple scattering Monte Carlo"). From the Mean Free Path and the rate of energy loss due to inelastic scattering as calculated with the Bethe [Bethe et al. 1930] or Joy-Luo [Joy et al. 1989] expressions, the loss of energy can be calculated along the path of the electron. After the electron travels a distance equal to the Mean Free Path, the next scattering site is reached, and a new scattering angle is chosen for the next step based upon the new value of the energy. Since the elastic scattering angle can take on any value

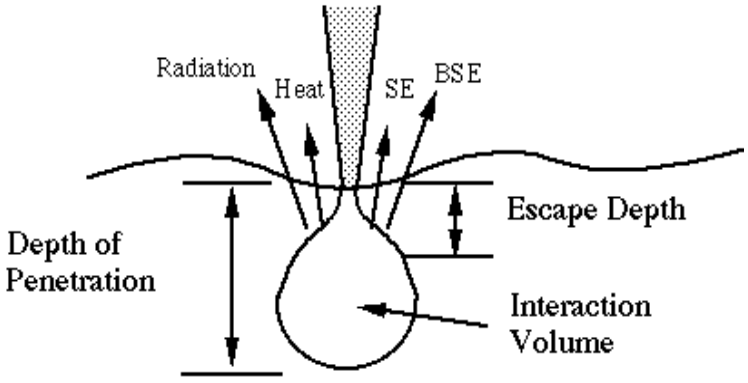


Figure 4.2 Physics processes encountered by electron.

over a wide range from 0 to 180 degrees, random numbers are used with an appropriate weighting factor to produce the appropriate statistical distribution of scattering. Because of the extensive use of random numbers in the simulation, the name "Monte Carlo" is applied to this technique.

4.2.2 Assumptions for Original Model

There are two major approximations based on which the original model was established.

(1) Only elastic scattering events described by the Rutherford cross-section are significant in determining the path taken by any given electron as it moves through the solid. As described in chapter I, there are essentially two kinds of the scattering, elastic scattering and inelastic scattering. The elastic scattering happens when the electrons repulsed by the orbital electrons of the nucleus while undergo the Columbic attraction from the positively charged nucleus of the target atom. During elastic scattering, a large range (5°~180°) of scattering angles could be covered [Edgerton 1996], though only less than 1eV energy loss from the incident electron to the target atom. On the other hand, the majority of the inelastic scattering produce angular deflections of typically 0.5° or less, but with large fraction of the energy loss. Consequently the elastic scattering dominate in determining the path of the trajectory of the electrons and ignoring the inelastic effects introduces only negligible error while greatly reducing the number of computations that may be required.

(2) The energy loss of the incident electrons is assumed to be a continuous process along their path at a rate determined by Bethe [Bethe et al. 1930] relationship, instead of as the result of discrete inelastic scattering events. In reality the continuous energy loss, such as Bremsstrahlung emission, and the discrete energy loss like Plasmons and Characteristic X-rays excitation created simultaneously, so Bethe average these energy loss processes and created Bethe relationship for the single scattering model [Bethe et al. 1930].

4.2.3 Statistics of the Original Model

Examination of the individual trajectories in Figure 4.3 (a output of the simulation) reveals that each trajectory varies greatly from any of the others because of the random selection from the range of scattering parameters.

Therefore the principal weakness of the Monte Carlo calculation is the need to calculate many trajectories in order to obtain statistical significance [Holt 1989]. In order to calculate results, which are representative of the overall interaction a statistically significant number of trajectories must be calculated. The precision of a Monte Carlo calculation depends on the number of events calculated, with the standard deviation of the calculation given by the expression:

$$SD = \sqrt{N_i} \qquad 4.4$$

Where N_i is the number of trajectories, which contribute to an event of type i. The relative standard deviations then given by

$$RSD = \frac{\sqrt{N_i}}{N_i} = \frac{1}{\sqrt{N_i}} \qquad 4.5$$

Thus in a calculation of a back scattering coefficient, the precision of the calculation is not determined by the total number of electrons calculated, N but by the number of electron which back scatter;

$$N_i = \eta N \qquad 4.6$$

In the same simulation, the calculation of characteristic X-ray production would be obtained with greater precision, since all of the incident electrons contribute to the generation of X-rays.

Why is Monte Carlo technique used so extensively? Most of the time, for each possible values and the probability distribution of the interested variable is always unknown in the case of reality. Although the statistical estimation could provide a value that is as close as possible to the actual unknown value, based on some definition of goodness or quality, the Monte Carlo simulation is always chosen since it can provide a

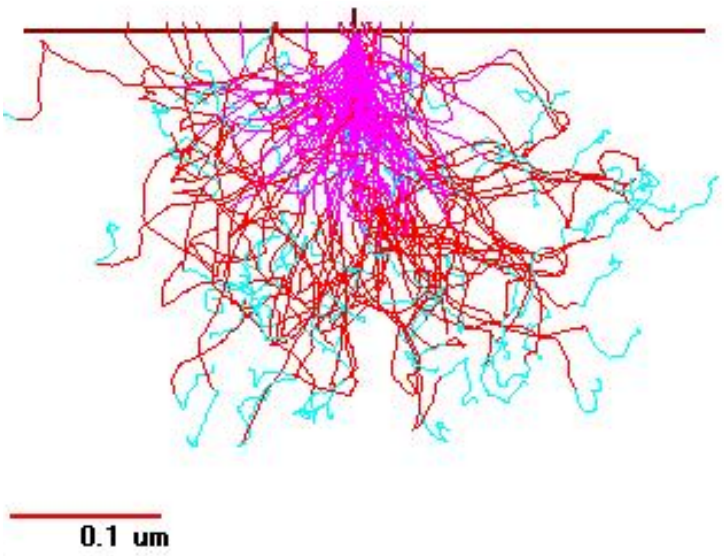


Figure 4.3 Monte Carlo simulation of the electron trajectories.

model uncertainty before and after a transfer function.

4.3 New Monte Carlo Simulation for Gas

4.3.1 Why Use This Method?

In the gaseous environmental SEM the incident electron beam is scattered when it passes through the low pressure gas atmosphere and results in a broadening of the electron probe, and a reduction in the current available for imaging and analysis. Moreover, the production of the secondary ions from the scattering can also impact the specimen and modify the production of secondary and backscattered electrons.

As we discussed before, to optimize and fully exploit the capabilities of gaseous environmental SEMs and the interaction between the electron beam and gas molecules, it is desirable to be able to accurately predict these effects of various micro-particles exists in the gaseous environment. An accurate model of the primary electron beam scattered in the gaseous environment would enable researchers to predict the magnitude of the scattered electron "skirt". Ideally the model would predict the optimum conditions to utilize efficiently the interaction between electrons and gas molecules and reduce the side effects on the analytical spatial resolution caused by scattering for a given gaseous system. Alternatively, it also would be used to develop a correction to the analytical data that reduces the effect of the scattered electron generated x-rays from the spectra. By using the Monte Carlo method and our measured cross-sections we can predict scattering profiles and compare these with our measured data.

Simple functional relations about these most concerned parameters could always be derived based on certain amount of assumptions. Based on this definition of the Mean Free Path length, at a gas pressure of 100 Pa, the Mean Free Path for 20 keV electrons is of the order of 1 cm. Therefore for a typical working distance of approximate 10mm, the average electron is only scattered once. Under this condition, one of the first approximation to the modification of the incident probe was established by estimating a mean scattering angle, Φ and assuming that this event occurs at the mid-point of the trajectory.

$$r^{\frac{1}{2}} = \frac{364.19Z}{E}\left(\frac{P}{T}\right)^{\frac{1}{2}} L^{\frac{3}{2}} \qquad 4.7$$

This equation has been adapted from the original version due to Reimer [1985] to include pressure and to be in SI units (E in eV). Goldstein [Goldstein et al. 1977] had previously derived the same formula except with a numerical factor 5.95 times larger. Smith and Schumacher [1974] have also produced a formula for the half width broadening given by

$$r^{\frac{1}{2}} = \frac{793.2}{\beta^2 (E + E_0)} \left[\frac{Z(Z+1)p}{T} \ln \frac{192\beta}{Z^{1/3}} \right]^{\frac{1}{2}} L^{\frac{3}{2}} \qquad 4.8$$

where

$$\beta = \left[1 - \frac{1}{\left(1 + \frac{E}{E_0} \right)^2} \right]^{\frac{1}{2}} \qquad 4.9$$

These relations have been demonstrated by several authors and represent a relativistic correction to give a useful estimate of the beam broadening [Farley et al. 1990].

However to quantitatively predict the behavior of the primary electron beam to adequately describe the beam profile as it reaches the specimen surface, a Monte Carlo simulation of should be a optimal choice. "GASSEM", a Monte Carlo simulation model was therefore developed.

4.3.2 How We Did It?

In our study, although the electron is scattered due to its collision with the gas molecule instead of solid molecule, the basic single scattering Monte Carlo model mentioned before could still be used because the gas is treated as a dilute solid here.

4.3.2.1 Include Inelastic and Elastic Scattering

In our new model, one major difference from the original model is that both the elastic and inelastic scattering events are included. Inelastic scattering has no effect on

the formation of the beam skirt because the scattering angles are too small by comparison with the elastic deflections. But inelastic events are crucial in determing the broadening of the focused probe.

The inelastic scattering was neglected and considered insignificant in determining the electron trajectory, because the deflection angle of the inelastic scattering is small (<1°). Due to the increasing requirement of the micro, even sub-micro scale products in the market, resolution of the technique in related development and research area is also becoming smaller and smaller. So the small angle scattering events are becoming causing more and more attention

In the small angle scattering area, the inelastic scattering events are in fact the majority of the scattering as indicated by Figure 4.4. It is also believed that it is the inelastic events, which determine the form of the beam profile close to (i.e. within a few micrometers of) the axis, and the relative higher angle elastic events determine the width and magnitude of the large scattered region which surrounds the beam [Joy 1995]. Therefore we can not ignore the inelastic scattering any more and both elastic and inelastic scattering will be included in the new model.

Since the scattering angle is so small for the inelastic scattering, it is relative difficult to obtain a set of inelastic scattering cross-sections by experiments based on our experiences. Moreover, most of the theoretical inelastic cross-section values derived based upon several approximations, which may not reliable for us to use in this model. Considering the possibility of the elastic scattering event is less than that of the inelastic scattering events, in the simulation, the ratio of inelastic scattering /elastic is selected by random numbers based on the assumption that the cross-section for inelastic scattering is some selected factor –typically 10 times of the elastic scattering cross-sections.

4.3.2.2 Single Scattering Model

It is also believed that in the regime of the interested collision of the incident electron beam and the surrounding gas molecules, the majority of the electrons still undergoing about one scattering event. So a single scattering model was established based on the original model by Joy [1995,1996] with some revision.

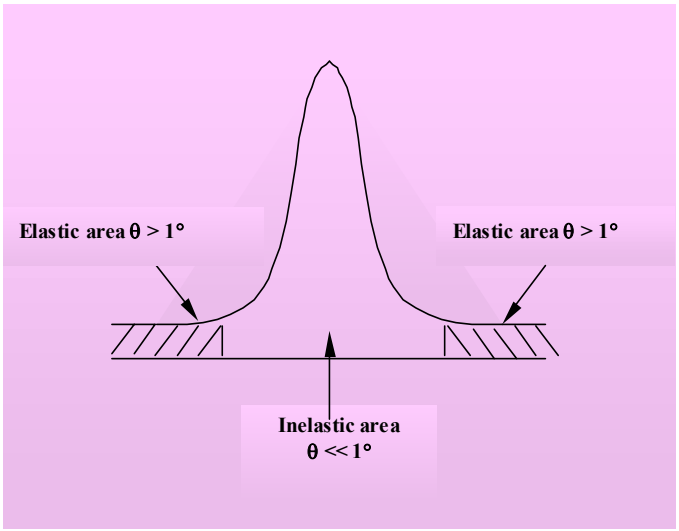


Figure 4.4 Schematic of the small angle scattering.

- The original single scattering model with Rutherford cross-section

The single scattering model Joy [1995] is the most accurate Monte Carlo simulation of the electron beam interaction is one which attempts to account for each elastic scattering event suffered by the electron as it travels through the sample [Newbury et al. 1981]. The single scattering model is also agrees well with experiments with large sampling base.

In this model, the system coordinate is established as illustrated in Figure 4.5. The electron is assumed undergoes an elastic scattering event at some point P_n, after having traveled from its previous scattering event P_{n-1}. The fundamental task of the simulation is to compute the coordinates of the point P_{n+1} to which the electron travels as a result of the scattering event at P_n. The parameters that could describe the instantaneous position of the electron are its energy E and the direction cosines of the trajectory segment that brought the electron from its previous scattering location P_{n-1} to P_n. These direction cosines, cx, cy, cz, are defined in a fixed set of axes attached to the specimen defined with the convention: the positive z-axis is normal to the specimen surface and directed in to the specimen, the x-axis is parallel to the tilt axis, the x-y plane is the surface plane of the untitled sample, and the y-axis completes a right handed set of axes
Based on the two approximations and the coordinates we discussed, the single scattering Mote Carlo simulation was created with the screened Rutherford elastic cross-section. The distance between P_n and P_{n+1} , the scattering Φ, and Ψ for the calculation of the new position of the scattering point P_{n+1}(xn,yn,zn) were all computed based on the Rutherford elastic cross-section.

The relativistically corrected screened Rutherford elastic cross-section σ_E used to compute the elastic scattering angles is given by

$$\sigma_E = 5.21\times10^{-21}\frac{Z^2}{E^2}\frac{4\pi}{\alpha(1+\alpha)}\left(\frac{E+511}{E+1024}\right)^2 \quad (\mathrm{cm}^2) \quad 4.10$$

where E is the electron energy (keV), Z is the atomic number of the target, and α is a scattering factor which accounts for the fact that the incident electron does not see all of the charge on the nucleus because of the orbiting electrons. Here the expression of α used

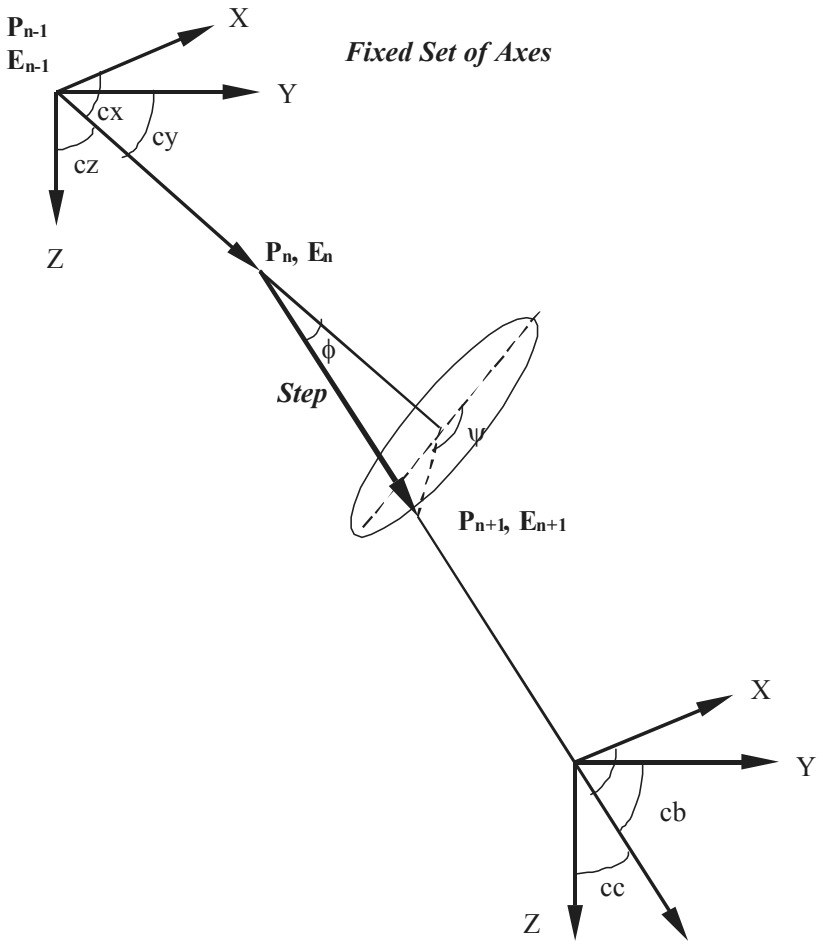


Figure 4.5 Coordinate system for Monte Carlo simulation

is [Bishop 1976]

$$\alpha = 3.4 \times 10^{-3} \frac{Z^{0.67}}{E^2} \qquad 4.11$$

With the elastic cross-section, the Mean Free Path λ could be computed by

$$\lambda = \frac{A}{N_a \rho \sigma_E} \qquad \text{(cm)} \qquad 4.12$$

where N_a is Avagadro's number, is the density (gm/cm^3) and A is the atomic weight(gm/mole). The value of Mean Free Path depends both on the beam energy and on the characteristics of the specimen, but is typically of the order of a few hundred angstroms at 100keV. The actual distance that an electron travel between successive scattering will vary in a random fashion, that is why we introduce this variability in the Monte Carlo simulation by saying that the step length between $P_n(x,y,z)$ and $P_{n+1}(xn,yn,zn)$ is given by the relation

$$\text{Step} = -\lambda \ln (\text{RND}) \qquad \text{(cm)} \qquad 4.13$$

Where RND is an uniformly distributed random number between (0, 1) automatically selected by computer.

In the scattering event at $P_n(x,y,z)$ which marks the start of this step, the electron is deflected through angle Φ (scattering angle) relative to its previous direction. This deviation is determined by the angular differential form of the Rutherford cross-section, $\sigma' = \frac{d\sigma_E}{d\Omega}$ and in our program is derived by solving

$$\text{RND} = \int_0^{\phi} \frac{\sigma'}{\sigma_E} \, d\Omega \qquad 4.14$$

where σ_E Rutherford elastic cross-section given before and integration extends to a maximum value of Φ. By evaluating Eq. 4.14, a formula can be derived [Newbury et al., 1976] which relates the random number RND with the scattering angle Φ,

$$\cos(\phi) = 1 - \frac{2\alpha \, \mathrm{RND}}{(1 + \alpha - \mathrm{RND})} \qquad 4.15$$

This equation could generate a unique scattering angle in the range of $0 \leq \Phi \leq 180$, producing an angular distribution which matches that obtained experimentally. Although and the majority of the scattering predicted by Eq. 4.15 is low angle scattering-that is less than 10°. The electron can scatter to any point on the base of the cone shown in the coordinate system in Figure 4.4, so similarly the azimuthal scattering angle could be given by

$$\Psi = 2\pi \, \mathrm{RND} \qquad 4.16$$

where RND is still a random number drawn automatically by computer.

With all the information available, Step, scattering angle Φ, azimuthal scattering angle Ψ, the scattering step from $P_n(x,y,z)$ to $P_{n+1}(xn,yn,zn)$ can be specified by the following equations:

$$xn = x + \mathrm{step}.\ ca \qquad 4.17a$$

$$yn = y + \mathrm{step}.\ cb \qquad 4.17b$$

$$zn = z + \mathrm{step}.\ cc \qquad 4.17c$$

where

$$ca = (cx.\cos\Phi) + (V1.V3) + (cy.\ V2.\ V4) \qquad 4.18a$$

$$cb = (cy.\cos\Phi) + (V4.(cz.V1 - cx.\ V2)) \qquad 4.18b$$

$$cc = (cz.\cos\Phi) + (V2.V3) - (cy.\ V1.\ V4) \qquad 4.18c$$

and

$$V1 = AN.\sin\Phi,\ V2 = AN.AM.\sin\Phi,$$

$$V3 = \cos\Psi,\ V4 = \sin\Psi \qquad 4.19a$$

$$AN = -\frac{cx}{cz} \qquad AM = \frac{1}{\sqrt{1 + AN^2}} \qquad 4.19b$$

Using this specified scattering step information of the primary electron, the step length "Step", scattering angle "Φ" and azimuthal scattering angle "Ψ" just derived, given a starting energy, new position and direction of the electron at "P_{n+1}" can then be tracked a step at a time.

- The new model with the experimental total scattering cross-section

One problem with the model created with the Rutherford cross-section though is when the energy of the primary electrons is low or when the atomic number of the target is high, the Rutherford cross-section are inaccurate because this theory has been derived in the frame of the first Born approximation [Gauvin et al. 1993]. Also, The Rutherford cross-section only accounts for elastic scattering event. Therefore in our single scattering model, the measured cross-section data we obtained in performed experiments is used instead of the Rutherford elastic cross-section to increase the accuracy of the simulation.

Although the measured cross-sections are supposed to be total scattering cross-section, as we discussed in last chapter, these cross-section values are actually elastic scattering cross-section only, because under the used experimental method, signals from the small angle inelastic scattering event could not be collected, which still results in the exclusion of the most part of the small angle inelastic scattering event.

Therefore, for elastic scattering event, the Mean Free Path, λ which was calculated by Eq. 4.12 should now be calculated by the revised Eq. 4.12′, where σ_M is the measured experimental cross-section:

$$\lambda = \frac{A}{N_a \rho \sigma_M} \qquad \text{(cm)} \qquad 4.12'$$

And for inelastic scattering event, the Mean Free Path is calculated based on the assumption of $\sigma_{IE} \sim 10\ \sigma_{IE}$ discussed above. Meanwhile, the inelastic scattering angle [Egerton 1996], θ is derived from

$$\theta = \frac{\Delta E}{E_o} \qquad 4.20$$

where ΔE is the energy loss in inelastic event. For the rest of the coordinate calculation, all the equations listed in the original model are employed.

4.3.2.3 Energy Loss of the Incident Electrons

So far we obtained the new position P_{n+1} under possible scattering event, either inelastic or elastic scattering for one step track, and whether the electron goes to next step will depend on the how much energy the electron still left.

As the electron travel through the solid its energy loses and since the scattering event is energy dependent, the instantaneous energy at any time need to be calculated. The energy loss, denoted by $\frac{\mathrm{dE}}{dS}$, could be given by the Bethe [1930] relation as:

$$\frac{\mathrm{dE}}{dS} = -78500 \frac{\rho Z}{AE} \log\left(\frac{1.166E}{J}\right) \qquad \text{(keV/cm)} \qquad 4.21$$

where J is the mean ionization potential which represents the average rate of energy transfer due to all possible inelastic events (i.e. the excitation of X-rays, Auger electron, phonons etc.). At high energies, E > 30 keV, it can be found from Berger and Selzer [1964] expression:

$$J = \left[\, 9.76Z + \frac{58.5}{Z^{0.19}} \right] 10^{-3} \qquad \text{(keV)} \qquad 4.22$$

However, at relative low energy, J also falls due to the possible attribution from the inelastic scattering events. To solve this problem, Joy and Luo [1989] rewrote the energy loss equation:

$$\frac{\mathrm{dE}}{dS} = -78500 \frac{\rho Z}{AE} \log\left(\frac{1.166E}{J} + 1\right) \qquad \text{(keV/cm)} \qquad 4.23$$

As demonstrated, this expression is accurate down to energies of 100eV only or below, and also avoids the difficulty in Eq. 4.21, that it can not be evaluated for E<J. Under both elastic and inelastic scattering events, the energy lost along the step, ΔE, from $P_n(x,y,z)$ to $P_{n+1}(xn,yn,zn)$ could be calculated using either Eq. 4.21 or 4.23 as:

$$\Delta E = \text{step} \left(\frac{dE}{dS} \right) \qquad 4.24$$

4.3.2.4 Schematic Sequence of the Operations

To summarize, the sequence of operations needed to simulate the electron path through the specimen can now be written out schematically in an algorithmic form:

Repeat
Get starting energy E of electron
Get starting coordinates x, y, z for the step
Get direction cosines cx, cy, cz relative to initial axes
Compute Mean Free Path for energy E and given material
Calculate the step length step from Eq. 4.13
Find the scattering angles from Eq. 4.15, 4.16 for elastic event,
Eq. 4.20 for inelastic scattering
Compute final coordinates xn,yn,zn from Eq.(4.17, 4.18, 4.19)
Compute finish energy E′=E – step(dE/ds)
Reset coordinates x=xn, y=yn, z=zn
Reset direction cosines cx=ca, cy=cb, cz=cc
Reset energy E=E′
Until electron leaves sample or falls below some minimum energy

This sequence of steps is repeated to simulate 30-60,000 electron trajectories as required by the desired accuracy.

4.3.2.5 I(r) Radial Beam Distribution Plot

The final simulation we built base on the original model accounts for the electron trajectory simulations of both elastic and inelastic scattering, permits all the experimental variables (gas composition, pressure and temperature; working distance and the accelerate beam energy) to be selected and tracks each electron from the point where it enters the low vacuum region until it reaches the sample surface, allowing the detailed beam profile to be determined.

Further more, the code for the real time graphic display of I(r) radial beam distribution is added for direct interpretation and applications of the scattering of the studied electrons. The inelastic and elastic regions are plotted separately.

Figure 4.6 is an example of the output of the final simulation code. The histogram shown in black color is the elastic beam scattering and the part of profile composed of red dot is the inelastic scattered beam profile. Strong inelastic scattering is evidence in the studied area. All the experimental conditions, such as applied accelerate voltage, the applied gas type and gas pressure, the used gas path length and chosen cross-sections. The corresponding data sets could easily be saved by checking the "Save" option in the interface.

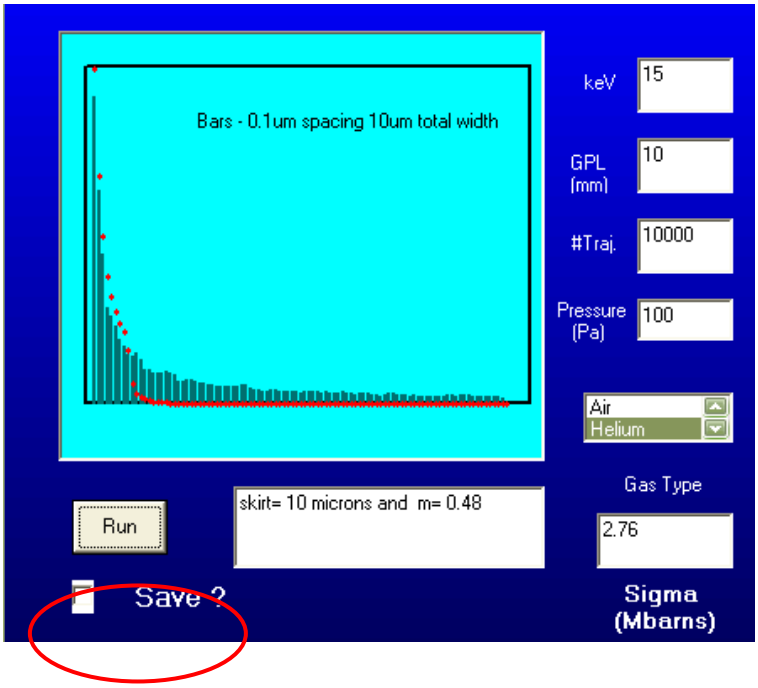


Figure 4.6 Interface of the simulation.

4.3.2.6 Computer Code

The computer code for this simulation, "GASSEM", to accomplish the whole sequence of operations is quite short and written in Visual Basic. The completed code is attached in the Appendix I.

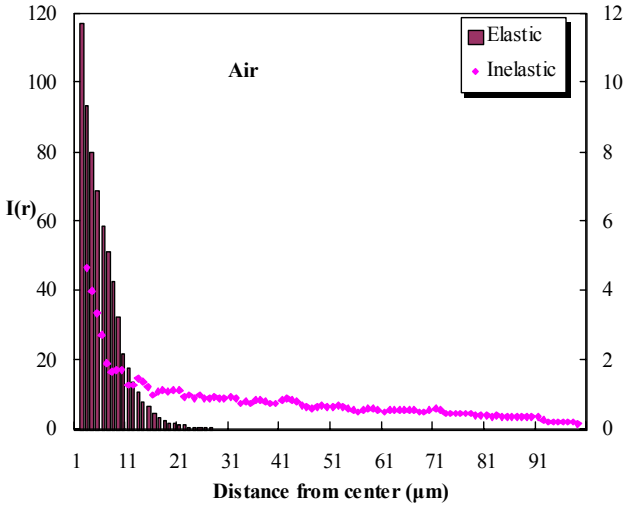
4.4 Simulation Results

Based on the saved data, the electron beam profiles can be replotted as shown in the following figures, which are some comparisons of the differences between electron beam scattering by different gas species, tested experimental conditions, and parameters applied in the simulation. The histogram in black color is the elastic beam profile in 1μm steps and the purple line profile is the inelastic scattered beam profile in 0.1μm steps.

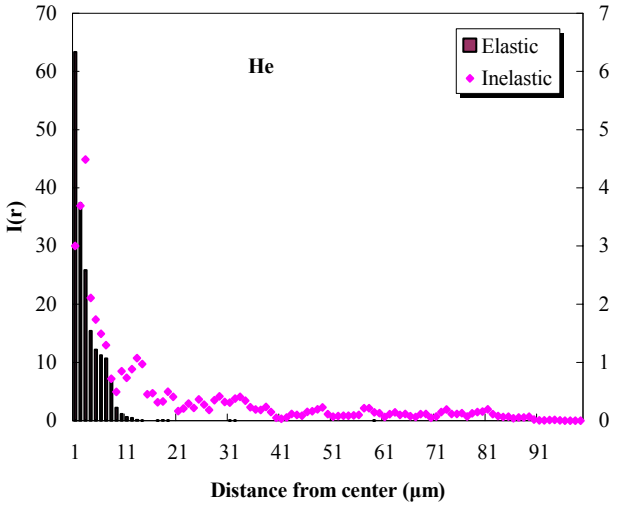
Figure 4.7 is one example for the comparison of the beam scattering by different gases. Due to the fact that the elastic scattering cross-section for air is almost 10 times larger than that of helium, as we mentioned in last chapter, the electron beam is scattered much stronger by anticipated air (a) than helium (b) as expected. Helium therefore is always an optimal choice used in the gas environmental SEM to reduce beam scattering or beam-gas interaction [Stowe 1998, Adamiak 2000].

The gas scattering is a strong function of gas pressure and applied accelerate voltage. The higher incident electron beam energy, the more difficult the electron beam is scattered, therefore lower degree of scattering is always expected in the higher beam energy case, here E=20kev (b) than the lower beam energy case, E = 10keV (a) as illustrated by Figure 4.8. The higher gas pressure presented, the more anticipated gas particles, which will result in the increasing of the beam scattering magnitude (Figure 4.9).

Since the elastic scattering and inelastic scattering can be simulated in the program, based on the assumption that the ratio of elastic scattering / inelastic scattering equals to 0.1, the ratio should be modified to achieve more accurate data of the gas scattering study. Figure 4.10 compares the simulation of two sets of applied inelastic / elastic ratios, 0.1 (a) and 0.15 (b). Multiple ratios should be applied in the simulation to obtain a large set of data to thoroughly explore the inelastic scattering event.

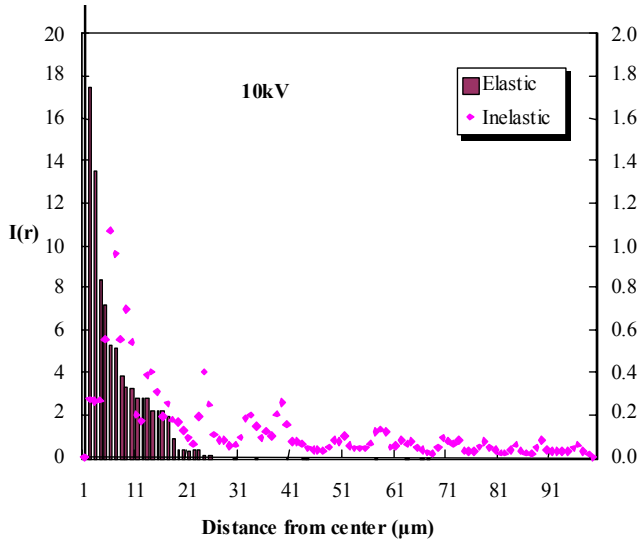


(a)

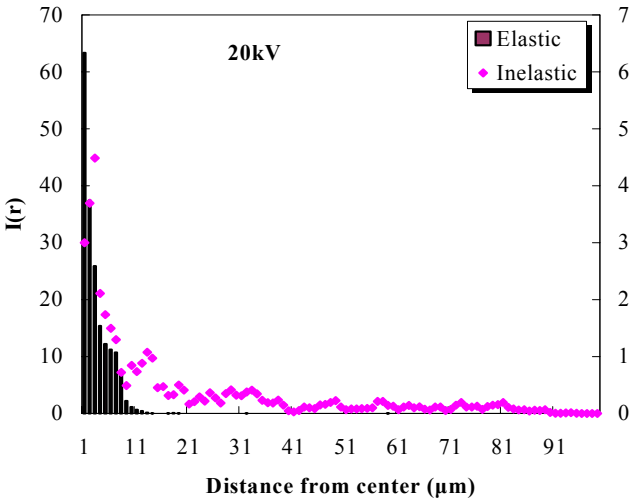


(b)

Figure 4.7 Comparison of beam scattering in air and helium at E = 20keV, P = 30Pa. (a) In air, (b) In helium.

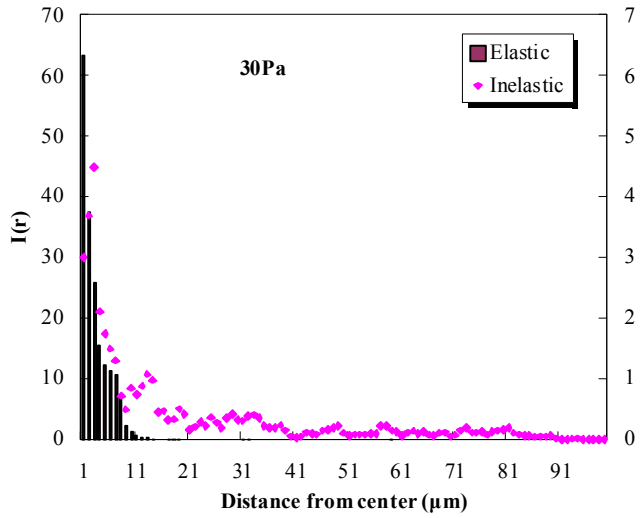


(a)

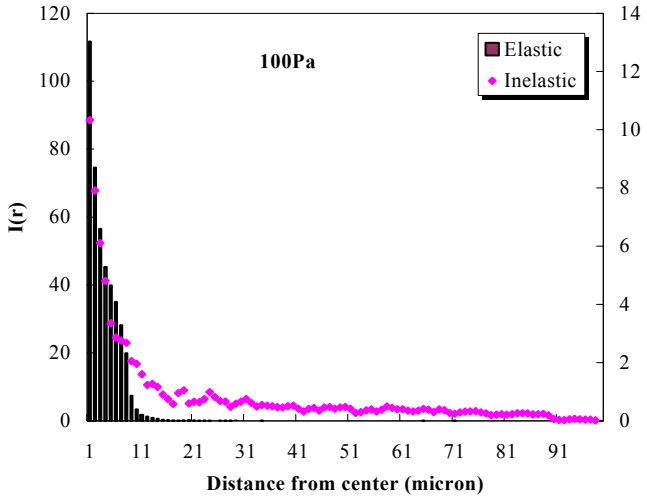


(b)

Figure 4.8 Comparison of beam scattering at E = 10keV, 20keV, P = 30Pa in helium. (a) E = 10keV, (b) E = 20keV.

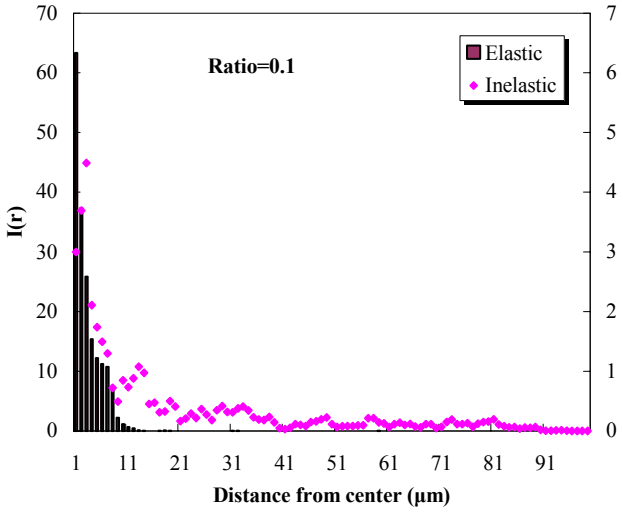


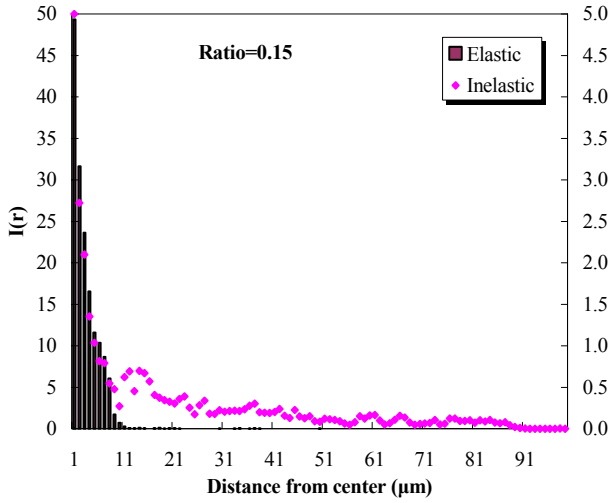
(a)



(b)

Figure 4.9 Comparison of beam scattering at P = 30Pa, 100Pa, E = 20keV in helium. (a) P = 30Pa, (b) P = 100 Pa.





(b)

Figure 4.10 Comparison of beam scattering with Ratio (inelastic/elastic) = 0.1 and 0.15 at E = 20keV, P = 30Pa. (a) Ratio = 0.1, (b) Ratio = 0.15.

As we discussed in chapter 3, the experimental obtained cross-section is almost 10 times the Mott's cross-section because in the studied pressure regime, many gases are believed to be molecular rather than atomic in nature. This fact is clearly evidenced in Figure 4.11. The beam scattering simulated based on the experimental cross-section is larger, due to the fact that the corresponding Mean Free Path (λ) is larger, which could result in more collisions between electrons and gas molecules, and so more scattering.

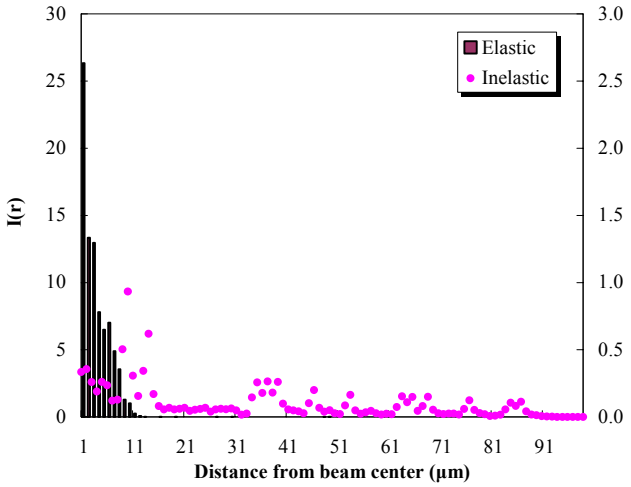
Finally the scattered electron beam radius from the Monte Carlo simulation model and the beam radius measured by P-N diode in chapter 2 are compared and both plotted in Figure 4.12 with the same conditions: beam energy = 25keV, GPL = 18.8mm, tested gas = Air. As compared to the theoretical value shown in red solid triangle in the plot, although both sets of radius values have the similar linear relationship with the $Pressure^{1/2}$, the beam radius obtained form the Monte Carlo model is much closer to the those theoretical data. This may due to the fact that in the Monte Carlo simulation, both inelastic scattering and elastic scattering are considered, while the profile measured by P-N diode only is able to capture the elastic scattering. The radius data for lower pressure region is not included here because there are still uncertainties which could not be explained well yet by the model and it is also the work will be done in the near future.

4.5 Summary

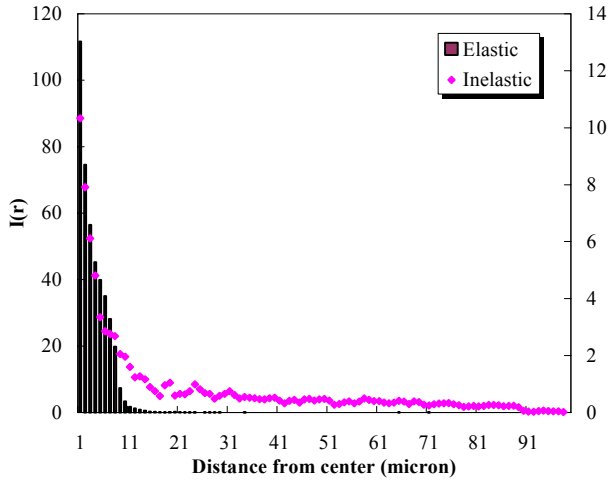
The Monte Carlo simulation model is established successfully by considering the gas as dilute solid. In this model, both elastic scattering and inelastic scattering events are included and plotted separately in the profile outputs.

With different sets of given conditions the model could predict the radial intensity distribution of the scattered electrons. Because we insert the obtained experimental total scattering cross-section into the simulation, more accurate beam broadening data could be achieved by the model for more thorough study of the electron beam scattering in the gas environmental SEM.

Meanwhile the simulation results from the Monte Carlo model illustrate our discussions about the deviation between the experimental cross-section and Mott's cross-section. The model also validates our suggestion about the existing gases, which is most of the anticipated gases in the procedure are believed to be molecular rather than atomic in nature.



(a)



(b)

Figure 4.11 Comparison of beam scattering with Mott's cross-section and experimental cross-section applied, at E = 20keV and P = 30Pa in helium. (a) Mott's cross-section applied in the simulation, (b) Experimental cross-section applied in the simulation

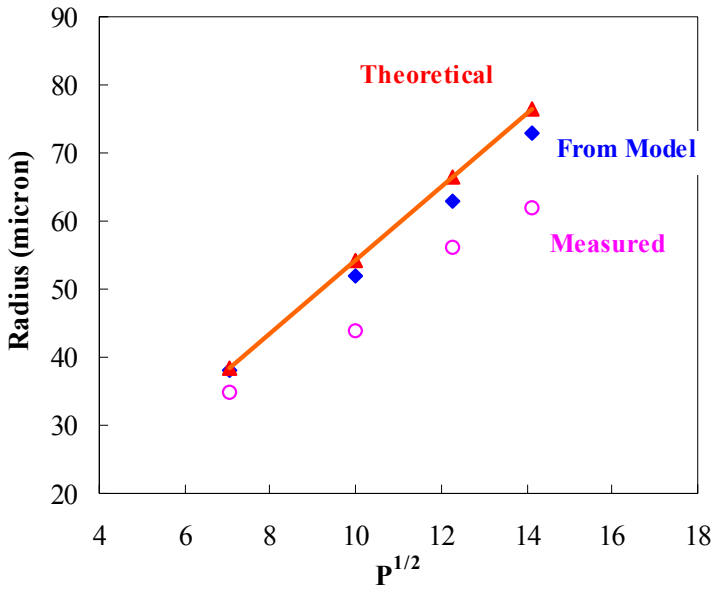


Figure 4.12 Comparison of the scattered electron beam radius obtained from the Monte Carlo model and P-N diode measurement in Air at E = 25keV.

REFERENCES

Adamiak B, Mathieu C: The reduction of the beam gas interactions in the variable pressure scanning electron microscope with the use of Helium gas, *Scanning*, Vol. 22, 178-181 (2000)

Berger MJ, Selzer SM: Studies in penetration of charged particles in matter, *Nat. Acad Sci natl Res Council publ*, Vol.1133, 205-228 (1964)

Bethe HZ: Theorie des Durchganges schneller Korpuskulerstrahlen durch Material, *Annalen de Phys.* (Leipzig), Vol.5, 325-333 (1930)

Bigelow WC: *Vacuum Methods in Electron Microscopy in Practical Methods in Electron Microscopy*, Vol.15, Portland Press, London (1994)

Bishop HE: in *Use of Monte Carlo Calculations in Electron Prove Microanalysis and Scanning Electron Microscopy* (Eds. KFJ Heinrich, Newbury DE and Yakowitz H (U.S. Dept. of Commerce/national Bureau of Standards), NBS Special Publication 460, 5 (1976)

Broers AN, Molzen WW, Coumo JJ, Wittle ND: Electron-beam fabrication of 80 Å metal structures, *Appl. Phys. Lett*. Vol. 29, 596 (1976)

Cazaux J. 1988

Coburn JW, Winters HF, J. Appl. Phys. Vol. 50, 646 (1987)

Danilatos G.D: Foundations of environmental scanning electron microscopy, *Advances in Electronics and Electron Physics*, vol. 71 (1998) 109-250.

Danilatos GD: Foundations of environmental scanning electron microscopy, *Advances in Electronics and Electron Physics*, Vol. 71, 109-250 (1988)

Danilatos GD: Theory of gaseous detector device in the environmental, *Advances in Electronics and Electron Physics*, Vol. 78, 1-109 (1990a)

Danilatos GD: Fundamentals of environmental SEM, *Eleventh Australian Conf. El. Microsc.*, University of Melbourne (1990)

Ditmire T: Atomic clusters in ultrahigh intensity light fields, *Contemporary Physics*, Vol. 38, 5, 315-328 (1997)

Edgerton R.F., *Electron Energy-Loss Spectroscopy in the Electron Microscope*, Plenum Press, New York (1996).

Engel VA: *Ionized Gases*, Clarendon Press, Oxford (1965)

Farley AN, Shah JS: primary considerations for image enhancement in high pressure scanning electron microscopy. Part 1. *J Microsc*, Vol. 158, 379-389 (1990a)

Farley AN, Shah JS: primary considerations for image enhancement in high pressure scanning electron microscopy. Part 2. *J Microsc*, Vol. 158, 390-401 (1990b)

Fiori CE, Swyt CR, Myklebust RL: DTSA – Desk Top Spectrum Analyzer (US Patent 529913) (1992)

Folch A, Servat J, Esteve J, Tejada J, Seco M: High-vacuum versus ‘‘environmental’’ electron beam deposition, *J. Vac. Sci. Technol*. B 14(4), 2609-2614 (1996)

Gauvin R, David C. Joy, On the Measurement of Total Elastic Cross-Sections in the ESEN or VPSEM using X-Ray Microanalysis, *Microscopy and Microanalysis* Vol. 6 (Suppl.2), 788-789 (2000)

Gauvin R, Drouin D: A formula to compute total elastic Mott cross-sections, *Scanning*, Vol. 15, 140-150 (1993)

Gauvin R, Griffin B, Nockolds C, Phillips M, Joy, DC: A method to measure the effective gas path length in the environmental or variable pressure scanning electron microscope, *Scanning*, Vol. 24, 171-174 (2002)

Gauvin R, Joy DC: On the measurement of total elastic cross-sections in the ESEM or VPSEM using X-ray microanalysis, *Microscopy and Microanalysis*, Vol.6 (Suppl.2), 788-789 (2000)

Gauvin R, L’Esperance G, St-Laurent S: Quantitative X-ray Microanalysis of Spherical inclusions embedded in a matrix using a SEM and Monte Carlo simulations, *Scanning*, Vol. 14, 37-48 (1992)

Gauvin R: Some theoretical considerations on X-ray microanalysis in the environmental or variable pressure scanning electron microscope, *Scanning*, Vol.21, 6, 388 (1999).

Gillen G, Wight S, Bright D, Herne T: Quantitative secondary ion mass spectrometry of self-assembled monolayer film for electron beam dose mapping in the environmental scanning electron Microscope, *Scanning*, Vol. 20, 404-409 (1998)

Goldstein JI, Costley JL, Lorimer GW, Reed SJB, *Scanning Electron Microscopy*, Vol. I, 315 (1977)

Goldstein JI, Newbury DE, Echlin P, Joy DC, Romig AD Jr, Lyman CE, Fiori C, Lifshin E: *Scanning Electron Microscopy and X-ray microanalysis*, Plenum Press, New York (1992)

Hebbard DF, Wilson PR: Austral. J. Phys., Vol. 8, 90 (1955)

Joy DC, Luo S: An empirical stopping power relationship for low-energy electrons, *Scanning*, Vol.11, 176-180 (1989)

Joy DC: Modeling the electron-gas interaction in low vacuum SEMs, *Microscopy and Microanalysis,* 468-469 (1996)

Joy DC: Modeling the electron-gas interaction in low-vacuum SEMs, *Microsc Microanal* (Eds. Bailey, Corbett, Dimlich, Micheal, Zaluzec) San Fancisco Press, 836-837 (1996)

Joy DC: *Monte Carlo Modeling for Electron Microscopy and Microanalysis*, OUP: NY, (1995)

KFJ Heinrich, Newburey DE and Yakowitz H (U.S. Dept. of Commerce/national Bureau of Standards), NBS Special Publication 46), 5 (1976)

Mathieu C: Principle and application of the variable pressure SEM, *Microscopy Analysis*, Vol. 13, 13-14 (1996)

Mathieu C: The beam-gas and signal-gas interactions in the variable pressure scanning electron microscope, Scanning Microscopy, Vol.13, No. 1, 23-41 (1999).

Matsui S, Lchihashi T, Mito M: Electron beam induced selective etching and deposition technology, *J. Vac. Sci. Technol*. B7 (A5), 1182-1190 (1989)

Matsui S, Mori K, *Appl. Phys. Lett*. Vol. 51, 646 (1987)

Matsui S, Mori K: New selective deposition technology by electron-beam induced surface reaction, *J. Vac. Sci. Technol*, B4, 299 (1986)

McDonald AM et al, Materials World, Vol. 6, no. 7, 399-401 (1998).

Metropolis N: The beginning of the Monte Carlo Method, *Los Alamos Science*, Special Issue, 125-130 (1987)

Mohan A, Khanna N, Hwu J, Joy DC: Secondary electron imaging in the variable pressure scanning electron microscope, *Scanning*, Vol. 20, 436–441 (1998)

Moncrieff DA, Barker PR, Robinson VNE, Harris LB: Electron scattering by gas in the scanning electron microscope, *J. Phys. D: Appl. Phys.,* Vol. 12, 481-488 (1979)

Moncrieff DA, Robinson VNE, Harris LB: Charge neutralization of insulating surfaces in the SEM by gas ionization, *J. Phys. D: Appl. Phys*., Vol.11, 2315-2325 (1978)

Montgomery DC: *Design and Analysis of Experiments*, 5th Edition, Wiley & Sons, (2000)

Newbury DE, Myklebust RL, Analytical Electron Microscopy (Ed. Geiss RH), San Francisco Press, San Francisco (1981)

Newbury DE, Yakowitz H, Myklebust RL: The NBS Monte Carlo program, in *Use of Monte Carlo Calculations in Electron Prove Microanalysis and Scanning Electron*

Microscopy (Eds. KFJ Heinrich, Newburey DE and Yakowitz H (U.S. Dept. of Commerce/national Bureau of Standards), NBS Special Publication 460, 151-164 (1976)

Newbury DE: Modeling electron beam interactions in semiconductors, in *SEM Microcharacterization of Semiconductor* (Eds. Holt DE, Joy DC) Academic Press, London (1989)

Oho E, Asai N, Itoh S: Image quality improvement using helium gas in low voltage variable pressure scanning electron microscopy, *Journal of Microscopy*, Vol. 49 (6), 761-763 (2000)

Paul B: Effects of gas pressure on low-pressure electron-beam lithography, *Scanning*, Vol. 19, 466-468 (1997)

R.F. Edgerton, *Electron Energy-Loss Spectroscopy in the Electron Microscope*, Plenum Press, New York (1996).

Reimer L: *Scanning Electron Microscopy*, Springer-Verlag, Berlin (1985)

Romer MJ, Araujo D, Garcia R: Energy-loss dependence of inelastic interactions between high-energy electrons and semiconductors: a model to determine the spatial distribution of electron-hole pairs generation, *Materials Science and Engineering*, Vol.b42, 168-171 (1996)

Schumacher BW: Ontario Research Foundation Physics Research Report No. 6604 (1968)

Smith RC, Schumacher BW, *Nucl. Inst. and Methods*, Vol. 118, 73 (1974)

Stowe SJ, Robinson VNE: The use of helium gas to reduce beam scattering in high vapor resource scanning electron microscopy application, *Scanning*, Vol. 20, 57-60 (1998)

Tang X: Quantitative measurements of charging in a gaseous environment, *Microscopy and Microanalysis*, Vol. 8 (Suppl 2), 1540-1541 (2002)

Toth M, Kucheyev SO, Williams JS, Jagadish C, Phillips MR, Li G (2000)

Toth M, Thiel BL, Donald AM, *J. Microscopy*, Vol.205, 86 (2002)

Wight SA Experimental data and model simulations of beam spread in the environmental scanning electron microscope, *Scanning*, Vol. 23, 320-327 (2001)

Wight SA: Beam size in the environmental SEM: A comparison of model and experimental data. *Microscopy Microanalysis* (suppl 2) 4, 298-299 (1998)

Wight SA: Direct measurement of electron beam scattering in the environmental scanning electron microscope using phosphor imaging plates. *Scanning*, Vol. 22, 167-172 (1999)

Yu XR, Hantsche H, *J. Electron Spectroscopy and Related Phenomena*, Vol.50, 19 (1990)

APPENDIX

“GASSEM” code wrote in Visual Basic

```
'This program computes the broadening an electron beam in a gas
'(c) Jing He November 2002
'Modified David Joy November 2002
'complaints, bug reports etc to djoy@utk.edu

Option Explicit         'declare all variables
Dim a_step, inc_energy, tilt, range, b, ga, s_en
Dim al, al_a, ak, er, lam_a, sg, sg_a
Dim x, y, z, xn, yn, zn
Dim center, BS_coeff, e_min
Dim two_pi, beam_range, estimate
Dim ca, cb, cc, cx, cy, cz
Dim nu, cp, sp, an, an_m, an_n, s_tilt, c_tilt
Dim h, i, j, k, the_value As Integer
Dim plot_test, r_val, rr_val, color_value As Integer
Dim traj_num, bs_yield, num, unscattered As Long
Dim at_num, at_wht, density, mn_ion_pot, m_t_step, del_E
Dim LH_edge, RH_edge, bottom, pressure, the_top
Dim plot_scale, center_x, center_y, radial, TOA
Dim bbroad, ddum, total_lambda, gas_sigma
Dim E(1 To 51) As Single
Dim radius(0 To 99) As Single
Dim rradius(0 To 99) As Single
Dim data_Z(1 To 15) As Single
Dim data_A(1 To 15) As Single
Dim data_rho(1 To 15) As Single
Dim data_Ec(1 To 15) As Single
Dim data_MABS(1 To 15) As Single
Dim theta, distance, GPL
Dim number, XRay_N, dot_density, E_crit
Dim no_color, chop, ID
Dim FileName As String

Private Sub Command1_Click()
   'the gas scattering program. Includes inelastic approximation
  Dim radius1, radius2, radius3, ll, total
  Dim fraction, test_type
  'clear the screen
  Picture1.Cls
  'reset the counters
  num = 0
  bs_yield = 0
  unscattered = 0
  fraction = 0.1  'ratio of elastic to total cross-section
  For i = 0 To 99 'zero the inner scale measure
   radius(i) = 0
```

```
    rradius(i) = 0
   Next i
 'get the data for this calculation
 'incident beam energy
   inc_energy = Val(Text1.Text)
 'get gas path length in mm
    distance = Val(Text2.Text) 'in mm
    GPL = distance * 1000 'put in microns
'number of trajectories to run
    traj_num = Val(Text3.Text)
    bbroad = 0.9 * traj_num
'gas pressure (in Pa)
    pressure = Val(Text5.Text)
'experimental gas total cross-section in Mbarns (10^-18cm2)
    gas_sigma = Val(Text6.Text)
'read the properties of the gas in the column
     the_value = List1.ListIndex
       If the_value < 1 Then the_value = 1
       If the_value > 14 Then the_value = 14
'and assign the values
      at_num = data_Z(the_value)
      at_wht = data_A(the_value)
      density = at_wht / 22400 'from Gas law
      density = density * (pressure / 101080) 'pressure in Pa

Call Berger_Selzer
Call gas_broadening

'get constants
 get_constants
       e_min = 0.5 '500eV minimum useful energy

'draw the screen and set up calibration rings
       Picture1.ScaleMode = 3 'set scale to pixels
       Picture1.BackColor = QBColor(15) 'white background

'set up the screen for plotting the display
    center_x = Picture1.ScaleWidth / 2
     LH_edge = center_x * 0.1
     RH_edge = center_x * 1.95
     center_y = Picture1.ScaleHeight / 2
    the_top = center_y * 0.15
 ' set up the plotting scale based on the estimated broadening
  'plot_scale is pixels per micrometer
       plot_scale = (Picture1.ScaleWidth * 0.75) / (estimate)

    ' as a first approximation ignore energy losses and compute
    ' a value for the total MPF from the experimental cross-section
```

```
total_lambda = 37700000000# / (gas_sigma * pressure) 'lambda in A, sigma in Mbarns

    inc_energy = Val(Text1.Text)

'reset the random number generator
Randomize

'****************************************
'****************************************
'******* the Monte Carlo loop  ************

 While num < traj_num
    x = 0
     y = 0
      z = 0
      cx = 0
     cy = 0
    cz = 1
    s_en = inc_energy
    color_value = 14
  'distance before first scattering event
    'a_step = -Lambda(s_en) * Log(Rnd) * 0.0001 'microns
     a_step = -total_lambda * Log(Rnd) * 0.0001 'microns
    zn = a_step
  'check the position of the electron now
     If zn > GPL Then 'this one hits the surface
      'Call xyplot(0, 0)   'plot at center
       unscattered = unscattered + 1
       radius(0) = radius(0) + 1
       rradius(0) = rradius(0) + 1
      GoTo jump2
      End If

  'reset the coordinates
      x = 0
      y = 0
      z = zn

 'now start the single scattering loop
       While s_en > e_min
       'a_step = -Lambda(s_en) * Log(Rnd) * 0.0001 'in microns
       a_step = -total_lambda * Log(Rnd) * 0.0001 'microns
       'now test the type of scattering
        test_type = Rnd
        If test_type <= fraction Then 'its elastically scattered
       Call s_scatter(s_en)
       GoTo next_step
       Else
       Call inelastic_scatter(s_en)
```

```
        End If
next_step:
        Call new_coordinates
      'now decide what happens next
         If zn < 0 Then
           bs_yield = bs_yield + 1
           GoTo jump2
        End If

         If zn > GPL Then 'this one hits the surface
         ll = (GPL - z) / cc 'length of exit vector
           xn = x + ll * ca    'exit x coordinate
           yn = y + ll * cb    'exit y coordinate
         'Call xyplot(xn, yn)   'plot it
        radial = Sqr((xn * xn) + (yn * yn)) 'exit radius from axis
        rr_val = Int(radial)  '1 micron annulae
        If rr_val < 99 Then
        rradius(rr_val) = rradius(rr_val) + 1#
        End If
         r_val = Int(radial * 10) '0.1 micron annular rings
           If r_val < 99 Then       'no overflow
             radius(r_val) = radius(r_val) + 1#      'add it
             End If
             GoTo jump2:  'finish this trajectory

         End If
      'otherwise go round again
         Call reset_next_step
      Wend     'end of the while loop
jump2:        'exit point

'*****************************************
'*****************************************
'********  end of the Monte Carlo loop ********

          num = num + 1
        If (num Mod 100 = 0) Then
            Randomize
        End If
      Wend      'end of the counter
            Call Plot_radial
            Call Plot_rradial
          'estimate 90% scattering radius

          ddum = 0
          total = 0
          For k = 0 To 99
           total = total + rradius(k) * (2 * k + 1)
          Next k
```

```
            total = 0.9 * total 'look for 90% value
            For k = 0 To 99
            ddum = ddum + rradius(k) * (2 * k + 1)
            If ddum >= total Then GoTo hiccup
            Next k
hiccup:

Text4.Text = "skirt= " & (k + 1) & " microns and " & " m= " & 0.01 * Int(100 *
unscattered / num)

   'and allow the data to be saved to disk if required
        'first give it a unique ID
        ID = Int(1000 * Rnd)
   If Check1 = 1 Then  'it will be saved
      FileName = "a:" & "Test" & ID
        Debug.Print "this file was "; FileName
         Debug.Print "  "
   'now write the file
      Open FileName For Output As #1
   'first save the inelastic data at 0.1 micron steps
    Write #1, "Inelastic data 0.1um steps"
    Write #1, "*********"
    For k = 1 To 99
     Write #1, (k * 0.1), "     ", radius(k)
    Next k
    'then save the elastic data at 1 micron steps
    Write #1, "          "
    Write #1, "Elastic data 1um steps"
    For k = 1 To 99
      Write #1, k, "    ", rradius(k)
    Next k
     Close #1

    End If
End Sub

Private Sub Form_Load()
'color the form to look nice
FadeForm Me, False, False, True
'load the data table
data_Z(1) = 7.2: data_A(1) = 14.5
data_Z(2) = 2: data_A(2) = 4
data_Z(3) = 14: data_A(3) = 28.02
data_Z(4) = 10: data_A(4) = 20.183
data_Z(5) = 12: data_A(5) = 24
data_Z(6) = 18: data_A(6) = 39.948
data_Z(7) = 16: data_A(7) = 32
data_Z(8) = 22: data_A(8) = 44
```

```
'set up the Materials list
    List1.AddItem "Choose one"
    List1.AddItem "Air"
    List1.AddItem "Helium"
    List1.AddItem "Nitrogen"
    List1.AddItem "Neon"
    List1.AddItem "Water Vapor"
    List1.AddItem "Argon"
    List1.AddItem "Oxygen"
    List1.AddItem "CO2"

'set up the list control
   List1.ListIndex = 0
'default values for error trap
    at_num = 6
    at_wht = 12.01
    density = 2.34
    TOA = 30 'detector take-off angle
    gas_sigma = 1  'cross-section in Mbarns
s_tilt = 0
c_tilt = 1
'set up the constant
two_pi = 710 / 113
'initialize text windows
 Text1.Text = 15     'default inc_energy
 Text2.Text = 10    'default GPL mm
 Text3.Text = 10000      'default trajectory number
 Text5.Text = 100       'default pressure 100Pa
 Text4.Text = "E-beam in Gas October 2002"
 Text6.Text = 10

center_x = Picture1.ScaleWidth / 2
LH_edge = center_x * 0.1
RH_edge = center_x * 1.95
center_y = Picture1.ScaleHeight / 2
the_top = center_y * 0.15
bottom = center_y * 1.55
plot_test = 0

End Sub

Private Sub FadeForm(frm As Form, Red%, Green%, Blue%)
Dim SaveScale%, SaveStyle%, SaveRedraw%
Dim i&, j&, x&, y&, pixels%

'save current settings
SaveScale = frm.ScaleMode
SaveStyle = frm.DrawStyle
SaveRedraw = frm.AutoRedraw
```

```
'paint screen
frm.ScaleMode = 3
pixels = Screen.Height / Screen.TwipsPerPixelY
x = pixels / 64# + 0.5
frm.DrawStyle = 5
frm.AutoRedraw = True
For j = 0 To pixels Step x
  y = 240 - 245 * j / pixels
    'can tweak if required
    If y < 0 Then y = 0
    'error trap
    frm.Line (-2, j - 2)-(Screen.Width + 2, j + x + 3), RGB(-Red * y, -Green * y, -
Blue * y), BF
Next j

'reset previous settings
frm.ScaleMode = SaveScale
frm.DrawStyle = SaveStyle
frm.AutoRedraw = SaveRedraw

End Sub

Public Sub gas_broadening()
  Dim T, E, estimate1, estimate2

 'estimate beam broadening using simple model
     T = 300                    'this is room temperature
      distance = distance * 0.001 'convert to meters
     E = inc_energy * 1000       'convert keV to eV
    'so the estimated beam broadening is
        estimate1 = 354 * at_num * distance / E
        estimate2 = estimate1 * Sqr(pressure / T)
        estimate = estimate2 * Sqr(distance) * 1000000 'converts to microns
        estimate = Int(estimate)
         'tidy up display
'display this value in a text box
         Text4.Text = "estimated broadening is " & estimate & "um"

End Sub

Public Sub Berger_Selzer()
    'calculates the mean ionization potential
    'using the Berger-Selzer fit with atomic number
        mn_ion_pot = (9.768 * at_num + (58.5 / at_num ^ 0.19)) * 0.001
End Sub

Public Sub s_scatter(energy)
    'calculates the scattering angles using
```

```
    'the screened Rutherford model
    Dim R1, al
        al = al_a / energy
        R1 = Rnd
        cp = 1# - ((2# * al * R1) / (1# + al - R1))
        sp = Sqr(1# - cp * cp)
        'and get the azimuthal scattering angle
        ga = two_pi * Rnd
End Sub

Public Sub new_coordinates()
'computes the new coordinates for the electron
'using the scattering angles found earlier
'transforms coordinates back to laboratory frame
Dim v1, v2, v3, v4
If cz = 0 Then cz = 0.000001 'error trap
    an_m = -cx / cz
    an_n = 1# / Sqr(1 + (an_m * an_m))
'get the transformation terms
    v1 = an_n * sp
    v2 = an_m * an_n * sp
    v3 = Cos(ga)
    v4 = Sin(ga)
'get the new direction cosines
    ca = (cx * cp) + (v1 * v3) + (cy * v2 * v4)
    cb = (cy * cp) + (v4 * (cz * v1 - cx * v2))
    cc = (cz * cp) + (v2 * v3) - (cy * v1 * v4)
'hence the new coordinates are
    xn = x + a_step * ca
    yn = y + a_step * cb
    zn = z + a_step * cc

End Sub

Public Sub reset_data()
'resets everything for the next step

 'first plot the last step
    Call xyplot(y, z, yn, zn)
    'reset the local variables
     cx = ca
      cy = cb
       cz = cc
       x = xn
      y = yn
     z = zn

'and compute the energy loss on that step
    del_E = a_step * stop_pwr(s_en) * density * 0.00000001
```

```
      s_en = s_en - del_E

End Sub

Private Function Lambda(inc_energy)
'calculates the elastic MFP

    al = al_a / inc_energy
    ak = al * (1# + al)
'giving the cross-section in cm^2 as
      sg = sg_a / (inc_energy * inc_energy * ak)
'and lambda in angstroms is
       Lambda = lam_a / sg

End Function
Private Sub reset_next_step()
'resets everything for the next step

 'first plot the last step
   ' Call xyplot(xn, yn)
    'reset the local variables
     cx = ca
      cy = cb
       cz = cc
       x = xn
      y = yn
     z = zn

'and compute the energy loss on that step
    del_E = a_step * stop_pwr(s_en) * density * 0.0001
      s_en = s_en - del_E

End Sub

Public Sub xyplot(a, b)
'plot the position of the electron as it hits sample
    Dim px, py, pxa, pya
        px = center_x + a * plot_scale
        py = center_y + b * plot_scale
         Picture1.DrawWidth = 3
        Picture1.PSet (px, py), QBColor(12)

        Picture1.DrawWidth = 1
End Sub

Private Sub get_constants()
'computes constants needed by the program

al_a = 0.00343 * at_num ^ 0.667
```

```
'relativistically correct the beam energy
er = (inc_energy + 511#) / (inc_energy + 1022#)
er = er * er

lam_a = at_wht / (density * 6E+23) 'lambda in cm
lam_a = lam_a * 100000000# 'put into angstroms

sg_a = at_num * at_num * 12.56 * 5.21E-21 * er

End Sub

Public Function stop_pwr(energy)
 'computer stopping power using modified Bethe law
 'the result is in keV/gm/cm^2
 If energy < 0.05 Then energy = 0.05
  stop_pwr = 78500 * at_num * (Log(1.166 * (energy + 0.85 * mn_ion_pot) /
mn_ion_pot)) / (at_wht * energy)

End Function

Public Sub inelastic_scatter(energy)
'computes the inelastic scattering angle assuming a single
'gas ionization event
   sp = 0.015 / energy
   ga = two_pi * Rnd
End Sub

Public Sub Plot_radial()
'plots the radius[rval](0.1um annulae) data to show beam broadening
Dim origin_X, origin_Y, volume
Dim prz_x, prz_y
Dim dummy2, dummy3
Dim cx, cy, cxx, cyy
Dim end_of_range As Integer

   Picture1.Cls
   ScaleMode = 3   'set scale to pixels
   Picture1.BackColor = QBColor(11) 'light cyan background
'set up the screen for plotting the display
      origin_X = LH_edge
      origin_Y = the_top
'plot the axes
      Picture1.CurrentX = origin_X
      Picture1.CurrentY = origin_Y
         Picture1.DrawWidth = 2
      'first mark in the major axes
      Picture1.Line (LH_edge, the_top)-(RH_edge, the_top), QBColor(0)
      Picture1.Line (LH_edge, the_top)-(LH_edge, 220), QBColor(0)
```

```
        'then complete the box
        Picture1.Line (LH_edge, 220)-(RH_edge, 220), QBColor(0)
        Picture1.Line (RH_edge, 220)-(RH_edge, the_top), QBColor(0)
        'finally some horizontal scale markers
        Picture1.CurrentX = 80
        Picture1.CurrentY = 45
        Picture1.Print "Bars - 0.1um spacing 10um total width"

'label the display
        cx = Picture1.ScaleWidth / 2     'scale independent
        cy = Picture1.ScaleHeight / 2

    'first normalize the radial data
        For k = 1 To 99
        radius(k) = radius(k) / (2 * k + 1)
        Next k
    'and smooth
        For k = 2 To 98
        radius(k) = (radius(k - 1) + 2 * radius(k) + radius(k + 1)) / 4
        Next k

    'now plot the radial intensity data

            Picture1.DrawWidth = 2
            dummy3 = 1 + radius(1) 'value of I(r) at first channel
            If radius(1) = 0 Then dummy3 = 1 'error trap
        For k = 1 To 99
         prz_x = LH_edge + 2.5 * (k + 1)
         prz_y = 220 - 200 * radius(k) / dummy3
         Picture1.Line (prz_x, 220)-(prz_x, prz_y), QBColor(3)
       Next k

End Sub

Public Sub Plot_rradial()
Dim ddummy2, ddummy3, prz_x, prz_y
 'first normalize the radial data
        For k = 1 To 99
        rradius(k) = rradius(k) / (2 * k + 1)
        Next k
    'and smooth
        For k = 2 To 98
        rradius(k) = (rradius(k - 1) + 2 * rradius(k) + rradius(k + 1)) / 4
        Next k
'plot the rradial intensity data (1 um annulae) as dots
            Picture1.DrawWidth = 3
            ddummy3 = rradius(1)  'value of I(r) at first channel
            If ddummy3 = 0 Then ddummy3 = 1 'error trap
        For k = 1 To 99
```

```
        prz_x = LH_edge + 2.5 * (k + 1)
        prz_y = 220 - 200 * rradius(k) / ddummy3
        Picture1.PSet (prz_x, prz_y), QBColor(12)
      Next k

End Sub
```

VITA

Jing He was born in Taiyuan, Shanxi in P. R. China on Jan. 20, 1974. She spent eighteen years in her hometown and graduated from high school in 1992 before she went to Beijing Science and Technology University. She received her B.A. in Material Science and Engineering in 1996 and continued her passion for Materials engineering in Central Iron and Steel Research Institute as an assistant engineer.

She came to United States on Christmas 1999 and started her graduate school in University of Tennessee from fall 2000. Since then she has been working in the EM lab of University as a research assistant. Under the instruction of Dr. David Joy she has been totally fascinated by the electron microscopy field, where she can always see things that never seen before. With her passion and hard work for her research, she received the Microbeam Analysis Society Distinguished Scholar Award in 2002.

In May 2003 she graduated from University of Tennessee with her M. S. in Material Science and Engineering and a Minor degree in Statistics.